Miner Deposita (2013) 48:697–728
DOI 10.1007/s00126-012-0450-3

ARTICLE

High-grade iron ore at Windarling, Yilgarn Craton: a product of syn-orogenic deformation, hypogene hydrothermal alteration and supergene modification in an Archean BIF-basalt lithostratigraphy

Thomas Angerer · Steffen G. Hagemann · Leonid Danyushevsky

Received: 12 March 2012 / Accepted: 19 November 2012 / Published online: 4 December 2012

Abstract Banded iron formation (BIF)-hosted iron ore deposits in the Windarling Range are located in the lower greenstone succession of the Marda–Diemals greenstone belt, Southern Cross domain, Yilgarn Craton and constitute a total hematite–martite–goethite ore resource of minimum 52 Mt at 60 wt.% Fe (0.07 P). Banded iron formation is interlayered with high-Mg basalts at Windarling and precipitated during episodes of volcanic quiescence. Trace element content and the rare earth element (REE) ratios Y/Ho (42 to 45), Sm/Yb (1.5), together with positive La and Gd anomalies in 'least-altered' hematite–magnetite–metachert–BIF indicate the precipitation from Archean seawater that was fertilised by hydrothermal vent fluids with a basaltic HREE-Y signature. Hypogene iron ore in sub-greenschist facies metamorphosed BIF formed during three distinct stages: ore stage 1 was a syn- to post-metamorphic, syn-D_1, Fe–Ca–Mg–Ni–Co–P–REE metasomatism that produced local Ni–REE-rich Fe–dolomite–magnetite alteration in BIF. Hydrothermal alteration was induced by hot fluid flow controlled by brittle–ductile reactivation of BIF-basalt margins and crosscutting D_1 faults. The Ni–Co-rich content of dolomite and a shift in REE ratios in carbonate-altered BIF towards Archean mafic rock signature (Y/Ho to 31 to 40, Sm/Yb to 1 to 2 and Gd/Gd* to 1.2 to 1.4) suggest that high-Mg basalts in the Windarling Range were the primary source of introduced metals. During ore stage 2, a syn-deformational and likely acidic and oxidised fluid flow along BIF-basalt margins and within D_1 faults leached carbonate and precipitated lepidoblastic and anhedral/granoblastic hematite. High-grade magnetite–hematite ore is formed during this stage. Ore stage 3 hydrothermal specular hematite (spcH)–Fe–dolomite–quartz alteration was controlled by a late-orogenic, brittle, compressional/transpressional stage (D_4; the regional-scale shear-zone-related D_3 is not preserved in Windarling). This minor event remobilised iron oxides, carbonate and quartz to form veins and breccia but did not generate significant volumes of iron ore. Ore stage 4 involved Mesozoic(?) to recent supergene oxidation and hydration in a weathering environment reaching down to depths of ~100 to maximum 200 m below surface. Supergene ore formation involved goethite replacement of dolomite and quartz as well as martitisation. Important 'ground preparation' for supergene modification and upgrade were mainly the formation of steep D_1 to D_4 structures, steep BIF/basalt margins and particularly the syn-D_1 to syn-D_2 carbonate alteration of BIF that is most susceptible to supergene dissolution. The Windarling deposits are structurally controlled, supergene-modified hydrothermal iron ore systems that share comparable physical, chemical and ore-forming characteristics to other iron ore deposits in the Yilgarn Craton (e.g. Koolyanobbing, Beebyn in the Weld Range, Mt. Gibson). However, the remarkable variety in pre-, syn- and post-deformational ore textures (relative to D_1 and D_2) has not been described elsewhere in the Yilgarn and are similar to the ore deposits in high-strain zones, such as of Brazil (Quadrilátero Ferrífero or Iron Quadrangle) and

Electronic supplementary material The online version of this article (doi:10.1007/s00126-012-0450-3) contains supplementary material, which is available to authorized users.

T. Angerer (✉) · S. G. Hagemann
Centre for Exploration Targeting, The University of Western Australia, Crawley, WA 6009, Australia
e-mail: thomas.angerer@uwa.edu.au

L. Danyushevsky
ARC Centre for Excellence in Ore Deposits, The University of Tasmania, Sandy Bay Campus, Geography-Geology Building, 333, Hobart, Tasmania 7001, Australia

Nigeria. The overall similarity of alteration stages, i.e. the sequence of hydrothermal carbonate introduction and hypogene leaching, with other greenstone belt-hosted iron ore deposits supports the interpretation that syn-orogenic BIF alteration and upgrade was crucial in the formation of hypogene–supergene iron ore deposits in the Yilgarn Craton and possibly in other Archean/Paleoproterozoic greenstone belt settings worldwide.

Keywords Southern Cross domain · Banded iron formation · Granite greenstone terrane · Geochemistry · Mineral chemistry

Introduction

The Windarling iron ore camp is located in the Windarling Range within the Marda greenstone belt, which is the southern part of the larger Marda–Diemals greenstone belt in the Southern Cross domain, Yilgarn Craton (Fig. 1a, b). The Windarling Range is defined by numerous, steeply dipping banded iron formation (BIF) units, which are between 10 and 50 m thick and predominantly surrounded by monotonous flows of metamorphosed high-Mg basalts (Figs. 1c and 2a). This rock series is here termed 'Windarling Formation'. The exact lithostratigraphic position of the Windarling Formation is unknown; it either belongs to the lower or upper association of the lower greenstone succession (cf., Riganti and Chen 2002).

Most of the known iron ore deposits in the Windarling Range are located in axial hinge zones of open-folded, east-southeast to east-northeast striking BIF units (Fig. 1c). The Windarling iron ore camp has a total (minimum) resource of 51.9 Mt (as of 2008, Portman 2008). The W2 deposit (10.1 Mt at 65.3 Fe and 0.07 P remaining reserve) is one of the major deposits and in the most advanced stage of mining. This paper describes the structural setting of the W2 deposit and the controls, paragenesis and chemistry of rocks and minerals in BIF alteration zones, magnetite–hematite ore and supergene iron ore. Ore genesis of other deposits in the Windarling Range remain speculative due to lack of data; however, the other three major high-grade (>58 wt.% Fe) iron ore deposits in Windarling (W1, W3 and W4) at least show similar ore types and structural characteristics.

Advances over the past 10 to 15 years in understanding the genesis of BIF-hosted high-grade iron ore have indicated the importance of Archean and/or Proterozoic hypogene 'ground preparation' of BIF (~35 wt.% Fe) prior to (Mesozoic? to recent) supergene upgrade in the formation of hematite or goethite–hematite ore (Barley et al. 1999; Taylor et al. 2001; Beukes et al. 2003; Dalstra and Guedes 2004; Cope et al. 2008; Figueiredo e Silva et al. 2008; Lobato et al. 2008; Angerer and Hagemann 2010). Also, structurally controlled, hypogene, high-grade iron ore formation is described in several deposits worldwide and in diverse geological settings (i.e. greenstone belt-hosted 'Algoma BIF' and basin-hosted 'Lake Superior BIF' setting). Several deposit-scale studies in the Southern Cross and Murchison domains and Narryer terrane within the Yilgarn Craton (Lascelles 2006; Angerer and Hagemann 2010; Duuring and Hagemann 2010; Maskell et al. 2012) show that BIF-hosted high-grade iron ore deposits preserved strikingly similar alteration sequences (Angerer et al. 2010). The studied deposits are hosted by greenschist (Koolyanobbing, Weld Range, Mt. Gibson) to lower amphibolite (Jack Hills) facies metamorphosed BIF, whereas the Windarling deposits in the Marda greenstone belt represents a sub-greenschist metamorphic end member setting of BIF. The studied Windarling deposits show a remarkable variety of ore textures, including porphyroclastic and porphyroblastic magnetite, anhedral/granoblastic and lepidoblastic hematite (lepH). This variability is reported from metamorphosed iron ore deposits in the Neoarchean Cauê Formation, Quadrilátero Ferrífero (Rosière et al. 2001, 2008), and possible similarities in ore genesis between both occurrences are discussed.

Regional geology of the Marda greenstone belt

The lithostratigraphy of the Marda greenstone belt is subdivided into a 3.05- to 2.93-Ga mafic rock- and BIF-rich lower greenstone succession (Cassidy et al. 2006) and a ca. 2.73-Ga upper greenstone succession, including felsic volcanic and volcanoclastic rocks of the Marda complex (2,732 ±3 and 2,734±4 Ma, U/Pb on zircons, Nelson 2002) and the clastic sedimentary rocks of the Diemals Formation (Riganti and Chen 2002; Chen et al. 2003; Cassidy et al. 2006). The upper greenstone succession uncomfortably overlies the lower succession, e.g. marking the northern boundary of the Windarling Range (Fig. 2a). Several gneissic zones in prominent shear zones (e.g. the Koolyanobbing, Mount Dimer and Evanston Shear Zones) and granites (e.g. at Butcher Bird Monzogranite, Pigeon Rock Monzogranite and Chatarie Well Granite; Fig. 1) are present in the central part of the greenstone belt (Fig. 2; also Jackson 1:100,000 map sheet, Riganti and Chen 2002). Granite domes

Fig. 1 **a** Overview map of the Yilgarn Craton (modified after Chen et al. 2003). **b** Overview map of the Marda–Diemals. *MDGB* Marda–Diemals greenstone belt, *HRGB* hunt range, *MMGB* Mount Manning. Shear zones: *ESZ* Evanston, *KSZ* Koolyanobbing, *MDSZ* Mount Dimer. Folds: *BA* Broadbents antiform, *BS* Bungalbin syncline, *DA* Diemals anticline, *HWA* horse well anticline, *WBS* Watch Bore syncline, *YS* Yarbu syncline, *BBM* Butcher Bird Monzogranite, *CF* Clampton fault, *DH* Deception Hill, *DHR* Die Hardy Range, *MJ* Mount Jackson Homestead, *PR* Pidgeon Rock granite, *CW* Chatarie Well Granite (modified after Chen et al. 2003). **c** Map of the Windarling Range (unplublished map kindly provided by CliffsNR Exploration) ▶

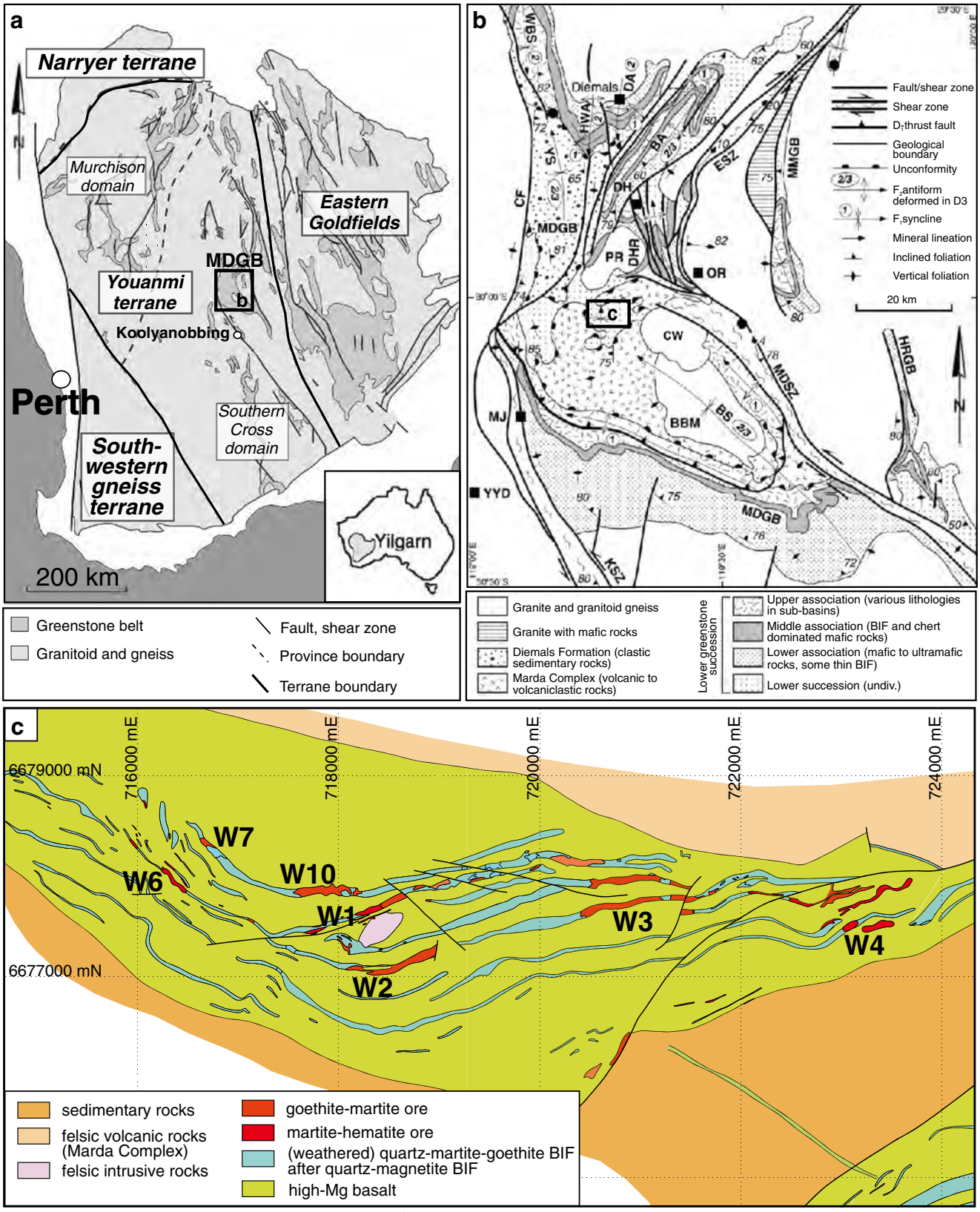

surround the greenstone belt and grade into gneisses and mylonite zones with proximity to shear zones.

The structural record in the central part of the Marda greenstone belt comprises three ductile deformation events (D_1 to

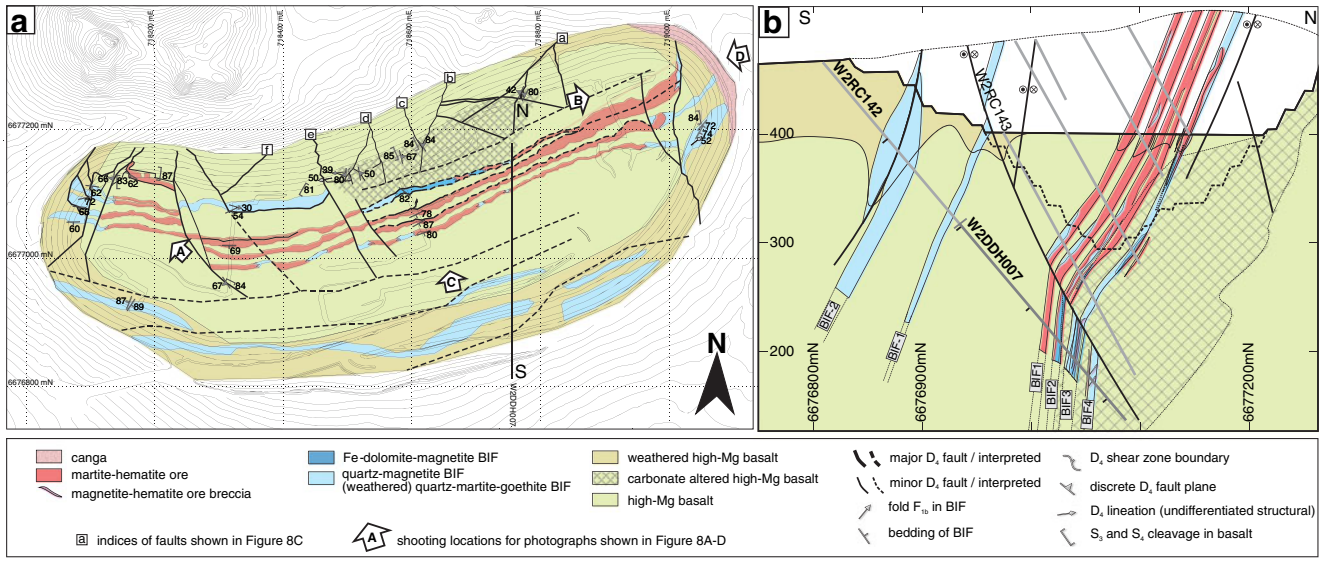

Fig. 2 W2 deposit maps and cross-section. **a** W2 deposit (pit topography as in early 2009). **b** N-S cross-section across deposit

D_3) followed by a series of late-stage, brittle–ductile to brittle deformation events, summarised as D_4 (Dalstra 1995; Dalstra et al. 1999; Chen et al. 2003). The D_1 is restricted to the lower greenstone succession, whereas D_2 to D_4 are recorded also in the Marda complex. A summary and comparison with the geological event history in the Koolyanobbing greenstone belt (Angerer and Hagemann 2010) and the central Southern Cross domain (Chin and Smith 1983; Dalstra et al. 1999; Riganti and Chen 2002; Chen et al. 2003) is given in Table 1.

The D_1 event involved the formation of layer-parallel foliation surfaces, thrusts and isoclinal folds in rocks of the lower succession. The BIF units are tightly to isoclinally folded showing intrafoliation folds within the BIF (Wyche et al. 2001). The D_1 took place in an originally north–south compressional stress field (Dalstra 1995). According to Riganti and Chen (2002), the age of D_1 is between 3.0 Ga, the approximate depositional age of the lower succession and 2.73 Ga, the extrusion age of the Marda complex.

The D_2 event involved the formation of small- to regional-scale upright folds, such as the Bungalbin syncline (Fig. 1), axial surface foliation in mafic rocks, thrusts and heterogeneous gneissic bands in granitoids mostly along granite-greenstone boundaries. The far-field stress during D_2 was broadly east–west oriented, and during this event east trending D_1 folds and thrusts were refolded, producing fold interference patterns at the outcrop scale (Dalstra 1995). In the Windarling Range, such a fold interference may have produced a buckling (banana shape) of the upright folded BIF units (Figs. 1c and 2a). The age of D_2 is broadly constrained to ca. 2.73–2.68 Ga, following the extrusion of the D_2-deformed Marda complex and late-stage granite intrusions, which intruded D_2 structures. The Diemals Formation is assumed to have been deposited syn-deformational with D_2 (Chen et al. 2003).

The D_3 event most likely represents of progressive deformation following D_2, because the east–west stress field remained the same during D_3 (Chen et al. 2001). This deformation produced transpressional, northeast-trending dextral and northwest-trending sinistral ductile shear zones along granite-greenstone belt boundaries, most prominently the Koolyanobbing, Evanston and Mount Dimer shear zones (Fig. 1). Gneissic bands and foliation in sheared monzogranite gneiss within the Koolyanobbing shear zone are truncated by northwest-trending sinistral shear zones, which suggests that major ductile deformation pre-dated transpressive shearing (Chen and Wyche 2001). The cessation of the D_3 event was between 2,656±3 (intrusion of the Lake Seabrook Granite at Koolyanobbing, Qiu et al. 1999) and 2,630±1 Ma (ductilely deformed pegmatites in the Lake Johnston greenstone belt, Joly et al. 2010).

The D_4 event is represented by large-scale north-northeast to east-southeast trending brittle shear zones and faults (Riganti and Chen 2002).

Main intrusive igneous activity in the southern to central Marda–Diemals greenstone belt was roughly synchronous with the Marda complex volcanism at ca. 2.73 Ga and, therefore, pre-to syn-D_2. The Butcher Bird Monzogranite and the Pigeon Rock Monzogranite are geochemically closely associated with the Marda complex volcanism (Nelson 2002; Riganti and Chen 2002). The Chatarie Well Granite intruded the Butcher Bird Monzogranite (Riganti and Chen 2002) and, therefore, may belong to a series of late- to post-kinematic granites, such as the monzogranite in the Evanston Shear Zone (2,654±6 Ma, Nelson 2002) or the Lake Seabrook Granite at Koolyanobbing.

Metamorphism within the Marda greenstone belt was temporarily associated with the main igneous activity in the region (Dalstra et al. 1999). Metamorphism took place in two stages, an early very-low- to low-grade seafloor and/

Table 1 Summary of the geological evolution of the Windarling area (Marda greenstone belt) and comparison with the Koolyanobbing greenstone belt (Angerer and Hagemann 2010) and the central Southern Cross domain (based on Dalstra et al. 1999)

		Central Southern Cross domain		Koolyanobbing greenstone belt		Windarling area (in Marda greenstone belt)	
Age in Ga	Tectonic regime	Tectonic event	Structures and P/T conditions	Tectonic event	Structures and P/T conditions	Tectonic event	Structures and P/T conditions
ca. 3.0	Basin	Deposition of the lower green stone succession throughout the Southern Cross domain					
	Burial			D_{1a}	Regional recumbent isoclinals folds, Low to moderate P/T conditions	D_{1a}	microscale extensional faults in BIF, diagenetic to very low grade
	N-S compression	D_1 (D_{1a}, D_{1b})	Regional detachments, moderate to low P/T conditions, Localised recumbent folds, moderate to high P/T cond.	D_{1b}	Localised upright to inclined folds, Low to moderate P/T condition	D_{1b}	localised tight to isoclinal folds, regional open east–west folds, low P/T conditions
2.73	Onset of orogeny					Marda complex eruption	
ca. 2.73–2.68	E-W compression (at Windarling: SW-NE)	D_2	Regional upright to inclined folds, low to high P/T conditions	D_{2a}	Regional upright to inclined folds, low to moderate P/T conditions	D_{2a}	Regional upright to inclined folds, low P/T conditions
				D_{2b}	Localised upright to inclined folds, brittle–ductile reverse shearing low P/T conditions (hydrothermal)	D_{2b}	Localised brittle–ductile reverse shearing along BIF-basalt contacts, very low to low P/T conditions
	End of syn-orogenic granitoids intrusions and metamorphism						
ca. 2.68–2.65	E-W transpression	D_3	Regional ductile transcurrent shearing, low to high P/T conditions	D_3	Not developed near Koolyanobb. deposits Localised ductile shearing (KSZ), low to moderate P/T conditions	D_3	Not developed near Windarling deposits Localised ductile shearing, low to moderate P/T conditions
				Onset of late- to post-orogenic granitoids intrusions Lake Seabrook granite (2,656±3 Ma, Qiu et al. 1999)		? Chatarie Well Granite (no age)	
		D_4	Regional transcurrent faulting, moderate to low P/T conditions	D_4	Localised brittle transcurrent faults Regional folds around vertical axis Regional cleavage, all low P/T conditions (hydrothermal)	D_4	Localised brittle reverse and transcurrent faults, very low P/T conditions
ca. 2.63	End of late- to post-orogenic granitoids intrusions						
	N-S compression	D5	Localised brittle reactivations and thrusting, very low P/T conditions	D_5	Localised brittle reactivations, very low P/T conditions		

or regional metamorphism producing prehnite–pumpellyite to greenschist facies assemblages, and a local medium- to high-temperature-peak metamorphic event during D_2/D_3, which was restricted to zones close to the main shear zones. The early regional metamorphic P/T conditions are constrained to about 300 °C and less than 180 MPa (Dalstra et al. 1999). No P/T information on subsequent hydrothermal events exists.

The W2 deposit—overview

The W2 deposit is situated in the centre of the Windarling iron ore camp (Fig. 1c). The 1-km-long and 300-km-wide deposit has a weakly arcuate shape with BIF striking east in the western part and east-northeast in the eastern part (Fig. 2a). The dominant high-grade iron ore type is magnetite–hematite–martite–goethite (martite is a pseudomorphic hematite after magnetite), which is located in four steeply south-dipping BIF bands (BIF 1 to BIF 4, Figs. 2a, b and 3a). In the eastern part, BIF 3 and BIF 4 join to form a single BIF 3 unit (Fig. 3d). Two unmineralised BIF south of the BIF 1 are named BIF 1 and 2. The BIF bands are partly truncated or offset by north trending faults at the western end of the open pit and covered by 'canga' (i.e. ferruginous detrital) at the eastern end (Fig. 3b). High-grade magnetite–hematite ore is intersected in all four BIF units well below the weathering front (70 m) in the drill hole W2DDH007 (Fig. 2b). A complex fault and shear zone pattern is developed throughout the deposit, with BIF bands being locally truncated and offset by an approximately north trending fault set (Fig. 3c). A dominant east to east-northeast trending set of discrete faults and broad shear zones strike parallel to the arcuate BIF.

A small felsic intrusive bodies, probably an apophysis of the Pidgeon Rock Monzogranite or Chatarie Well Granite, is exposed in the central part of the area, less than 500 m north of W2 (Fig. 1c). To the north, the Windarling Formation is unconformably overlain by felsic volcanic rocks of the Marda complex (about 2 km north of W2). In the south of the deposits, overlaying rocks are a clastic sedimentary rock dominated series (about 1 km south of W2).

Deformation and metamorphism in the W2 deposit

Bedding and diagenetic D_{1a} structures

S_0 In the Windarling Range, the BIF compositional layering is parallel to BIF unit boundaries, and therefore considered to be parallel to bedding S_0. The S_0 dips steeply towards the south, and locally the overturned beds dip towards north (Fig. 4a).

D_{1a} Earliest structures recorded in BIF units within the Windarling Range are centimetre- to decimetre-scale extensional faults with parallel magnetite veins (locally replaced by martite; Fig. 5a). These veins are locally folded in decimetre- to metre-scale folds. Meter-thick fault zones, hosting metachert and magnetite porphyroblasts (both similar to the wall rock BIF mineralogy) and locally microplaty hematite (mplH), crosscut bedding-parallel compositional

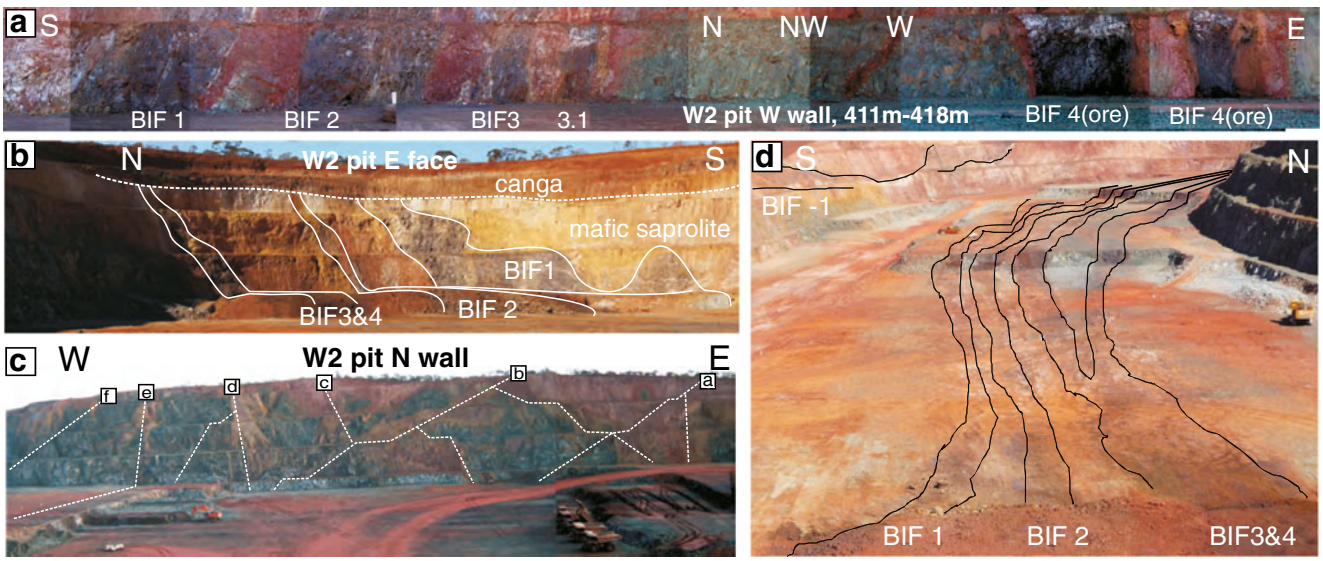

Fig. 3 The W2 open pit (photos taken from locations shown as *arrows* in Fig. 2). **a** West wall (411–419 m), showing unmineralised BIF 1 to BIF 3 and mineralised BIF 4; **b** East wall with BIF 1 to 4 covered by Tertiary(?) canga. **c** North wall displaying a complex D_4-fault pattern and associated weak weathering of wall rock basalt. **d** View from (**e**) showing the four parallel, mostly mineralised, BIF units (1 to 4) which are currently mined and two further unmineralised hanging wall BIF units (−1 and −2) in the southern pit wall

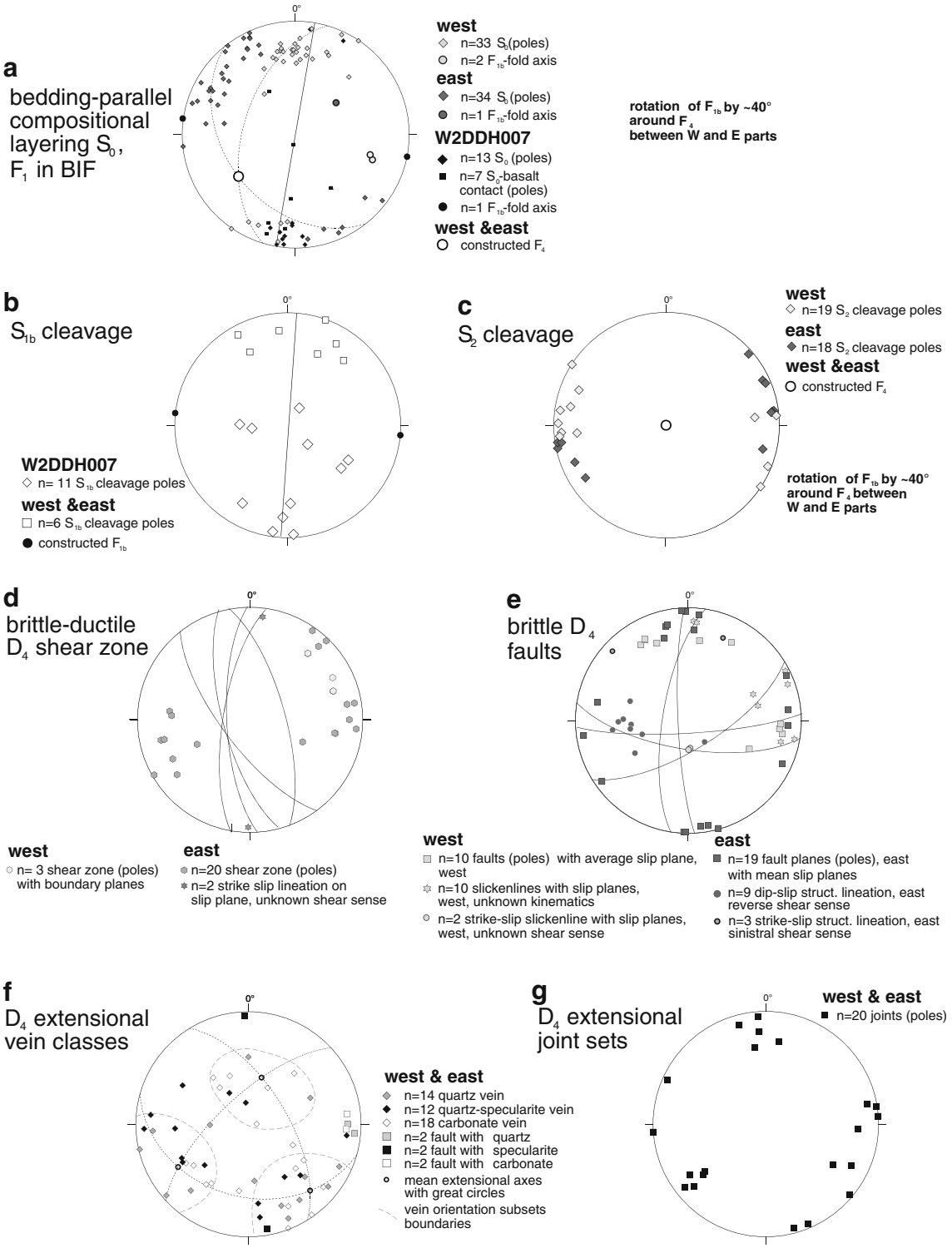

Fig. 4 Structures in the W2 deposit displayed in equal area projection of the lower hemisphere. **a** BIF compositional layering (parallel to bedding S_0), BIF-mafic rock contacts, and small-scale F_{1b} in BIF: both are rotated around a steep axis (F_4); **b** S_1 cleavages in mafic rocks and BIF; **c** S_2 cleavage in mafic rocks are rotated around a vertical F_4 axis; **d** brittle–ductile shear zones in mafic; **e** brittle faults in mafic rocks; **f** mineralised veins and faults; and **g** extensional joint sets

layering in BIF 4 in the W2 deposit. Magnetite in these veins and faults shows no textural difference to the metamorphic magnetite that commonly forms metamorphic iron oxide layers, suggesting a common metamorphic history, hence a syn-regional metamorphic relative minimum age for the veins. Because, regionally, D_1 is

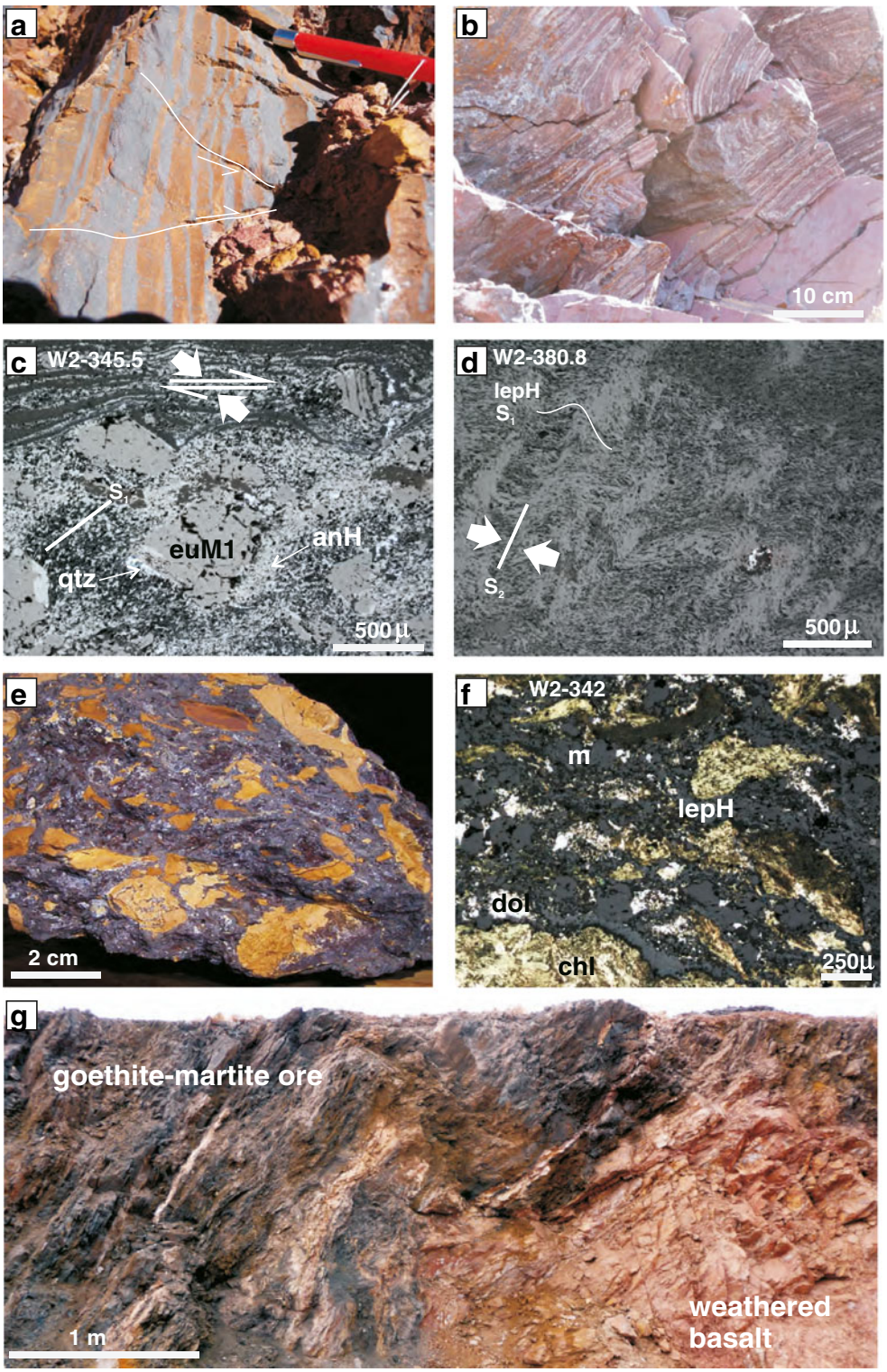

Fig. 5 Structures in the W2 and W3 deposits: **a** extensional D_{1a} faults displaying iron-oxide 'mud' was mobile between BIF layers before metamorphic and hydrothermal magnetite growth occurred; **b** D_{1b} folds in BIF 4 showing a layering-parallel axial surface; **c** photomicrograph (reflected and transmitted light) of a least-altered quartz–magnetite–hematite BIF showing magnetite porphyroblasts (euM1), which are locally rotated in layering-parallel shear zones, anhedral hematite (*anH*) in high-strain zones, and quartz (*qtz*) in pressure fringe (BIF 3, sample *W2-345.5*); **d** photomicrograph (reflected and transmitted light) of magnetite–hematite ore with domains of crenulations cleavage S_2 that overprints a typically layering-parallel cleavage S_{1b}, consisting of lepH (BIF unit 4, *W2-380.8*); **e** weathered medium-grade ore-basalt contact breccia, with brown clasts of weathered basalt in a matrix of magnetite–martite–hematite (courtesy R. Schellekens); **g** photomicrograph of a medium-grade ore-basalt contact breccia, showing lenses of chlorite and Fe–dolomite in a matrix of magnetite, hematite, and Fe-dolomite (*W2-342*); **g** sheared contact between tectonically folded and supergene-crinkled, leached, goethite–martite ore and weathered basalt, cropping out in the W3 west wall

considered as a N-S compression (cf., Dalstra 1995; Wyche et al. 2001; Riganti and Chen 2002), it is inferred that the present extensional veins are relicts of local mobilisations of iron oxide during a late diagenetic stage (D_{1a}), pre-dating main D_1 burial.

D_{1b} structures (metamorphic, pre-Marda complex)

F_{1b} In several places within the W2 deposit, layering in BIF is tight to isoclinally folded around fold axes that are sub-horizontal and east–west striking (Fig. 5b), therefore parallel

to the main fold axis which caused upright folding of the BIF units. Poles to layering surfaces define two great circles with axes plunging in ESE (for the western pit) and NE direction (for the eastern pit). This rotation of axes by about 40° is a result of a later refolding by a steep F_4, which led to a regional (Fig. 1c) to local, open pit-scale (Fig. 2a) 'banana-shape' buckling of the BIF units. With respect to the identification of folded early D_{1a} faults, this regional upright fold system is termed F_{1b} and is consistent with regional D_1 folding (Table 1; cf., Dalstra 1995; Wyche et al. 2001; Riganti and Chen 2002). An angular unconformity is interpreted for the footwall contact of the post-D_1-deposited Marda complex (Riganti and Chen 2002), but there are no outcrops along the boundaries of the Windarling Range that show a clear contact relationship to overlying rocks of the Marda complex. Therefore, it can only be assumed that the upright folding of the BIF units is the result of F_1.

S_{1b} The ductile folding of the BIF led to shearing parallel to the compositional layers and the formation of a S_{1b} cleavage, which is oriented parallel at a low angle to the layers (Fig. 5c). The growth of fine-grained, anhedral and lepH defining the cleavage surfaces is commonly observed (Fig. 5c, d). Metamorphic magnetite porphyroblasts (see below) are rotated during layer-parallel shearing and associated pressure fringes are developed and filled with comb quartz (Fig. 5c). In basalts, an incipient cleavage is defined by chlorite with a shape-preferred orientation. This S_{1b} cleavage in basalt and chlorite schist strikes east–west and dips, as a fan-like axial-planar fabric, shallowly to steeply to the north (Fig. 4b). Chloritised basalt and locally chlorite schist were generated by this syn-deformational alteration.

The D_{1b} event was most likely contemporaneous with regional, very low-grade burial metamorphism that predated the Marda volcanic complex (at 2.73 Ga). Regionally observed contact metamorphism in the vicinity of batholiths (Ahmat 1986; Mueller and McNaughton 2000) is not developed in the Windarling Range, mainly because of its setting distal to the intrusions.

D_2 structures (metamorphic, post-Marda complex)

F_2 The Windarling Range is located in the northern limb of the Bungalbin syncline, a post-Marda complex F_2 structure that is oriented in the eastern part subparallel to F_{1b} fold axes, but less well defined in the western part (Fig. 1b; Chen et al. 2001, 2003). At Windarling, the Bungalbin syncline trends north–south, hence is orthogonal to F_{1b} (Fig. 1b; Chen et al. 2001, 2003), which caused a lobate outcrop pattern of the folded Marda complex at the regional scale (Fig. 1b). Ductile to cataclastically reactivated BIF-basalt contacts host medium-grade (45–55 wt.% Fe) ore breccias, display chloritised and schistose basalt clasts in a magnetite–martite–hematite matrix, which may have formed as early as D_2 (Fig. 5e, f).

S_2 A second foliation in BIF, oblique to S_1, crenulated the earlier foliation (Fig. 5d), without showing significant growth of new hematite. The S_2 in BIF and iron ore has only been observed in breccias clasts, suggesting that this deformation was protracted and involved cataclasis at its late stage. In basalts, S_2 is roughly east–west trending and steeply dipping, and rotated by a maximum of 40° around a vertical F_4 (Fig. 4c). It is uncertain, if F_2, being orthogonal to F_{1b}, led to the cross-folding pattern in the Windarling Range and W2 open pit. The vertical, low-amplitude buckling of BIF units (Figs. 1c and 2a) may have been established as early as D_2, but large-scale rotation of S_2 around a subvertical F_4 (from eastern to western open pit) suggests a post-D_2 buckling.

D_3 structures (regional metamorphic, transpressional)

The Bungalbin synclinal domain represents an intermediate structural domain between sinistral, northwest trending Koolyanobbing and Marda–Diemals shear zones and the dextral, northeast trending Clampton fault and the Evanston shear zone (Fig. 1a, b). This domain is devoid of major D_3 transpressional deformation (Chen et al. 2001, 2003), which explains why the Windarling Range did not develop any ductile strike-slip structures, and was not rotated from any pre-D_3 orientation.

D_4 structures (brittle post-metamorphic)

All brittle and brittle–ductile structures, post-dating D_2, in mafic rock are subsumed under D_4. Most prominent are discrete faults (centimetre to decimetre width and metre width) shear zones with discrete boundaries and internal fracture cleavage. These D_4 structures crosscut BIF units (roughly north–south strike) or are located along BIF-basalt margins (east–west strike), where they host medium-grade (~45–58 wt.% Fe) and high-Al ore breccias with chloritised basalt clasts (Fig. 5f).

Shear zones Shear zones in the W2 open pit predominantly strike north to northwest (Fig. 4d). Subhorizontal slickenlines are rarely developed and indicate transcurrent kinematics. Variously oriented fracture S_4 cleavage in shear zones suggests overall compressional modes of shearing.

Faults Discrete strike-slip and dip-slip fault surfaces of metre to decametre scale, oriented north–south and east–west, are common throughout the W2 pit. Subhorizontal lineations, including slickenlines, fibres and rough surfaces direction indicate predominantly sinistral kinematics in

east–west and minor north–south direction. Minor faults include reverse and normal dip-slip types.

D_4 veins and joint pattern Extensional veins in basalts are mostly filled with quartz carbonate, less frequently with associated spcH. The orientations of these undeformed veins cluster in three domains (Fig. 4f). Locally, in the northern open pit wall, faulted veins host undeformed quartz, carbonate and specularite (Fig. 4f). Also syn-kinematically deformed en-echelon quartz–calcite–dolomite±spcH vein arrays are observed. A late-stage extensional three-set joint pattern is approximately parallel to the D_4 fault pattern (Fig. 4g).

BIF and iron ore petrography

The main host rock to the iron ore is a quartz–hematite–magnetite BIF, which is observed in the unweathered W2DDH007 drill core (Fig. 6b). In the open pit, BIF is mostly present with a weathered quartz–martite–hematite–goethite assemblage. BIF grain sizes vary from fine (<20 μm metachert and amalgamated magnetite/martite; Fig. 7c and left part of Fig. 7i) to coarse-grained (sub-millimetre size granular quartz and euhedral to amalgamated, magnetite/martite grains, Fig. 7a, b). Grain sizes vary laterally in individual BIF units.

A carbonate-magnetite BIF (Fig. 7d–g) is present below the weathering front and intersected by W2DDH007 diamond core (Fig. 6a). Carbonate-rich BIF is also exposed in a 200-m-long section of BIF 4 in the central-eastern part of the open pit (Fig. 2a). Pervasive carbonate alteration surrounding magnetite–hematite iron ore is common beneath the weathering front at depths below ~80 m (intersected by W2DDH007 in BIF 1, 2 and 3; Fig. 6). Alteration fronts of carbonate replacing metachert (Fig. 7i) are undeformed, hence neither significant volume reduction (>10 %) nor collapse brecciation occurred during carbonate alteration. This clearly suggests an isovolumetric carbonate replacement reaction without prior porosity-generating removal of metachert bands. BIF rich in Mg–Ca–Fe silicates that are expected to result from the reaction of SiO_2 and carbonate are not observed.

The main ore types are magnetite–hematite ore beneath the weathering front (Fig. 6a) and martite–hematite–goethite ore in the weathering zone (Fig. 7j). Textures in magnetite–hematite ore are either laminated, showing thinned, low-porous dolomite-rich layers (Fig. 7f) or brecciated with magnetite–hematite-rich matrices and clasts (Fig. 7h). Laminated martite–hematite ore appears to represent supergene-modified (oxidised) magnetite–hematite ore. In the open pit, martite–goethite ore formed by leaching of gangue is locally kinked due to gravitational collapse (Fig. 7i). metre-scale goethite-rich pods in BIF are observed in spcH-rich zones (Fig. 7k).

Mafic rock petrography

In high MgO (10 to 16 wt.%), metabasalts represent the hanging wall and footwall rocks to the BIF units at the W2 deposit. Metabasalts are massive, light to dark green, fine- to medium-grained rocks, which are either undeformed (Fig. 8a, e) or contain a weak chlorite cleavage (Fig. 8c, d)

The main constituent in the basalts is chlorite (~80 % of the rock volume) having replaced or partly replaced plagioclase and Mg–Ca–Fe silicates, such as olivine, pyroxene and amphibole (Fig. 8f, g). Chlorite commonly defines a cleavage and is most intensely developed between the BIF units and along sheared BIF/basalt contacts (Fig. 8c, d, h). Primary (titano-)magnetite phenocrysts are mostly replaced by leucoxene (Fig. 8a). The spcH–quartz–dolomite veins are most common in the hanging wall of BIF 1, whereas Fe–calcite–quartz veins are located in the footwall of BIF 4 (Fig. 8e, k). In the central northern part in the W2 open pit, carbonate vein and wall-rock alteration is most prominent (Fig. 2). Between BIF units, fewer veins (typically quartz–dolomite–spcH rich) are observed; however, close to the iron ore/basalt contacts, chlorite–magnetite–pyrite veins are common, crosscutting mafic rocks and sheared magnetite–hematite–pyrite ore (Fig. 8c, h). In the weathering zone (from the surface to depths of ~30 m), basalt is altered to light brown, friable saprolite. Moderately weathered reddish-brown saprock extends to greater depths (~80 m) and where it is intersected by faults (Fig. 8b, d), or along BIF-basalt margins (Fig. 3c). Within a meter close to BIF bands and to faults, clay minerals and cryptocrystalline hematite (crxH) developed due to weathering resulting in reddish to yellowish colour of basalt.

Several zones of medium-grained, holocrystalline olivine-plagioclase dolerite in the hanging wall of BIF 1 represent dikes that intruded the basalts (Fig. 8b). The dolerite is only moderately altered with olivine locally replaced by chlorite and plagioclase locally replaced by saussuritic minerals assemblages (Fig. 8i, j).

Paragenetic mineral sequence in BIF and ore

In the W2 deposit, a diagenetic to metamorphic and contact metamorphic, three distinct hydrothermal alterations (early, intermediate and late) and one supergene stage, each with distinct paragenetic assemblages have been determined (Fig. 9).

Regional metamorphic BIF assemblages

Cryptocrystalline hematite, anhedral magnetite-1 and metachert This assemblage forms the least-altered BIF in the

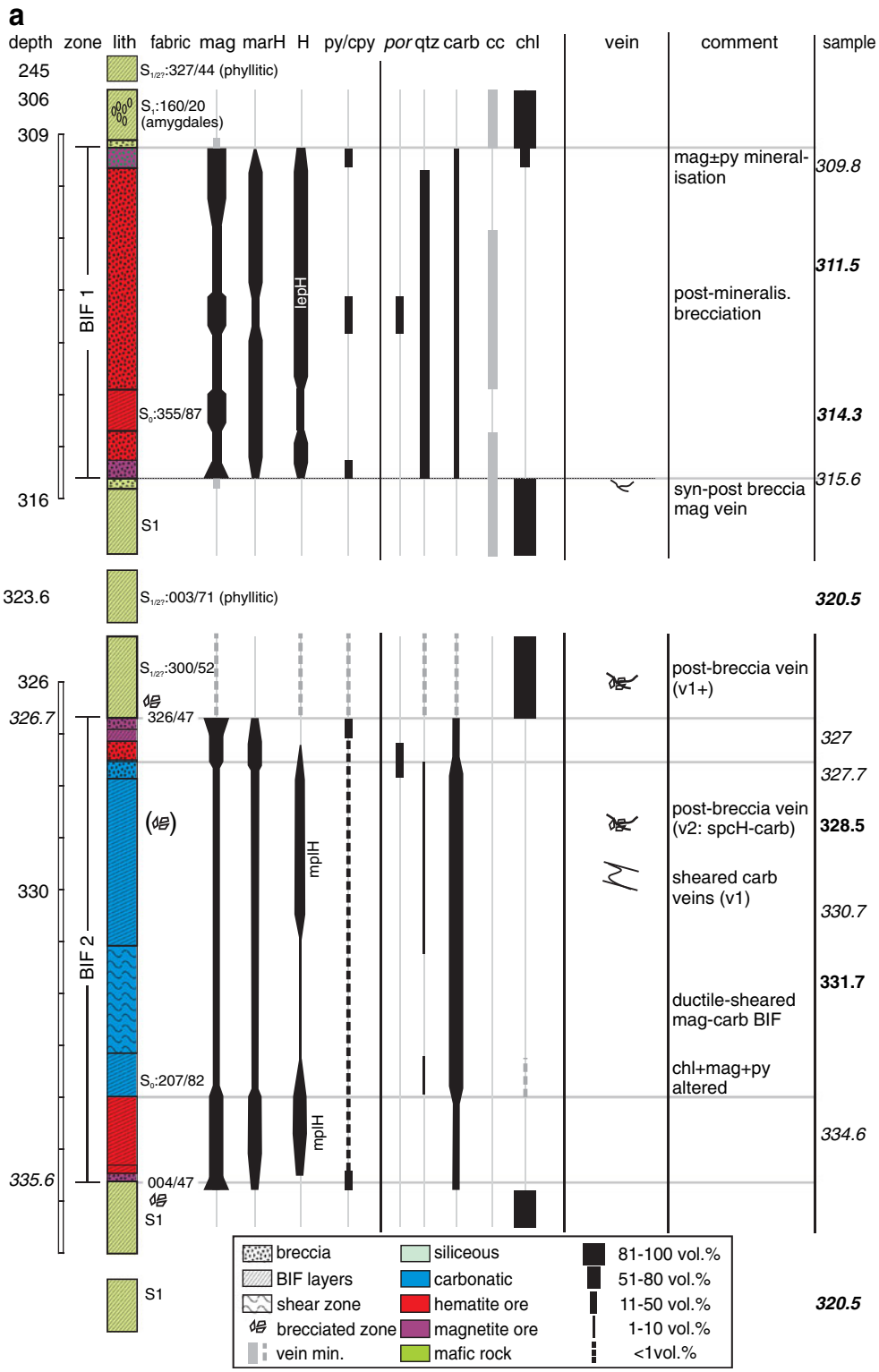

Fig. 6 Graphical log of the W2DDH007 diamond core that intersects BIF units 1 to 4. It shows lithology, alteration, structures, mineralogy of BIF and intercalated mafic rocks

Windarling Range and in deposits. In quartz–hematite layers, reddish, clay-size crxH impregnates metachert (Fig. 10a) that is <20-μm sized. In iron oxide layers, anhedral, amalgamated (i.e. a polycrystalline texture of anhedral and annealed crystals), magnetite-1 (anM1) dominates over metachert–quartz (Fig. 10b). The anM1 also occurs in medium- to high-grade magnetite–hematite ore. Replacement textures of anM after crxH (Fig. 10d) allows a judgment on the relative timing of the iron oxide species; also, an early crxH formation prior to anM1 may be supported from the virtual absence of oxidation of magnetite to martite.

Fig. 6 (continued)

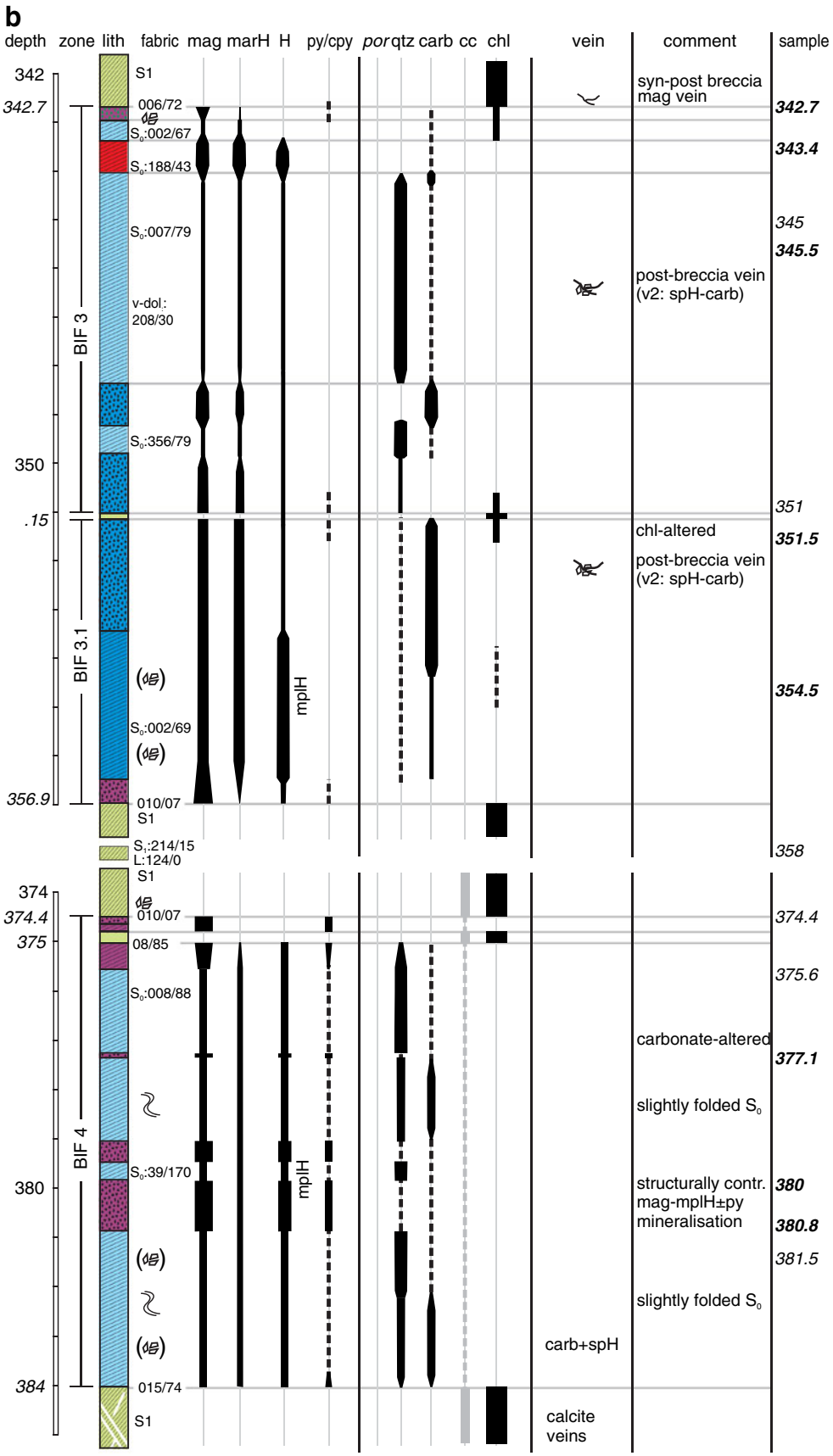

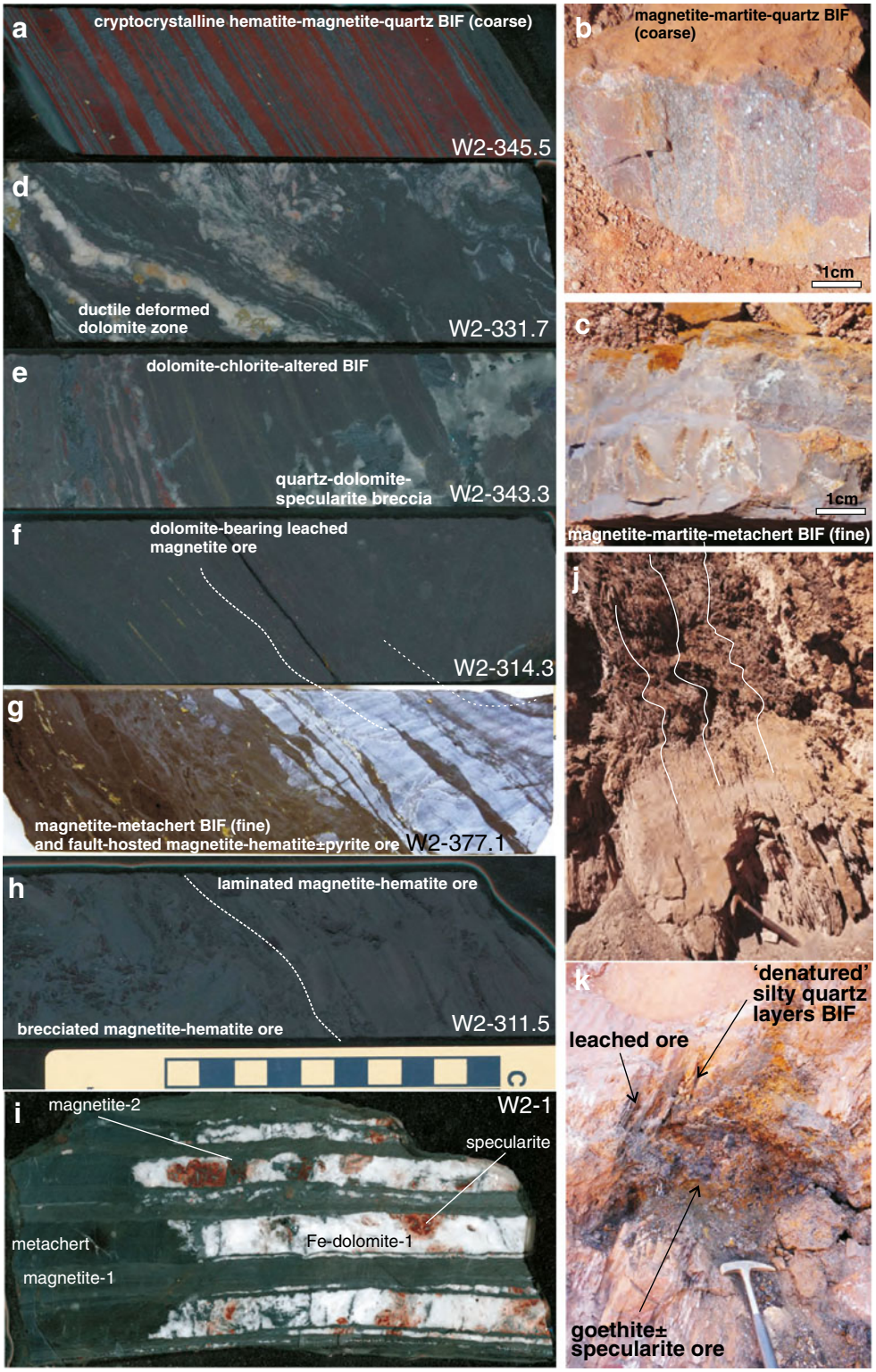

Fig. 7 BIF and ore types in the W2 deposit: **a** least-altered quartz–hematite–magnetite BIF (BIF 3, sample *W2-345.5*); **b** weakly weathered coarse-grained quartz–magnetite–martite BIF; **c** fine-grained metachert magnetite–martite BIF; **d** Fe–dolomite–magnetite BIF, ductile deformed (BIF 2, *W2-331.7*); **e** Fe–dolomite–magnetite BIF with spcH–Fe–dolomite–quartz pod at the *right side*, and reddish oxidised zone at the *left side* (BIF 3, *W2-343.3*); **f** laminated and thinned medium-grade Fe–dolomite–magnetite ore (BIF 1, *W2-314.3*); **g** contact between fault-hosted magnetite–hematite±pyrite ore-breccia and folded metachert–magnetite–hematite BIF (BIF 4, *W2-377.1*); **h** porous and partly brecciated high-grade magnetite–hematite ore (BIF 1, *W2-311.5*); **i** complex alteration in metachert-magnetite BIF 4 (sample *W2-1*): *dark grey* metachert intercalated with magnetite layers (*left side*). White sparitic Fe–dolomite replaced metachert and patches of hydrothermal magnetite and spcH (with reddish halos of hematite-stained carbonate) subsequently replaced Fe–dolomite. **j** BIF to martite–goethite ore transition outcropping in W3 pit, ore is crenulated due to gravitational collapse of leached gangue bands; **k** a spcH–goethite pod in a zone of strongly weathered ('denatured' metachert) and partly leached BIF

Local contact metamorphic mineral coarsening in BIF

Euhedral magnetite-1 and quartz-2 Subsequent to the formation of the crxH–anM1–metachert assemblage, large euhedral magnetite porphyroblasts (euM1; 500 μm to 1 mm) grow in iron oxide layers replacing crxH or form growth zones around anM1 (Figs. 5c and 10a–c). Sugary quartz-2 (100–500 μm) usually accompanies euM1 in coarse-grained BIF (Fig. 7a, b). Mineral chemistry indicates no significant difference between anM1 and euM1 (see below). This fact and the

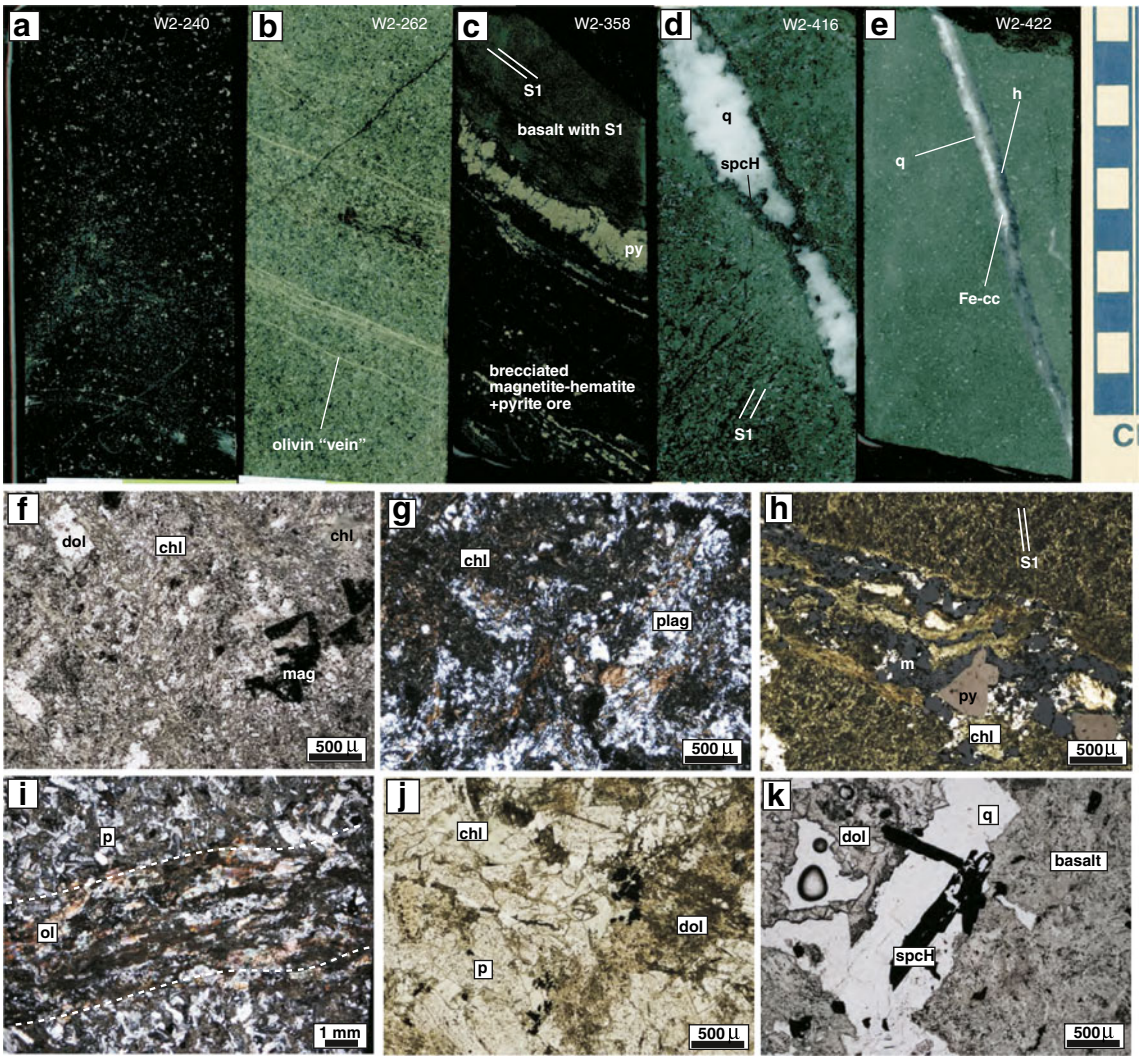

Fig. 8 Mafic wall rocks in the W2 deposit: **a** medium-grained chloritised basalt with light leucoxene spots; **b** partly chloritised olivine–plagioclase dolerite with characteristic sheeted olivine 'veinlets'; **c** chlorite-schist with S_1 cleavage at a magnetite–hematite–pyrite mineralised ore/basalt contact; **d** chloritised, schistose basalt with crosscutting quartz (*q*)-calcite (*cc*)-specular hematite (*spcH*) vein; **e** chloritised basalt with crosscutting q–Fe–calcite (*Fe-cc*)–crxH (*h*) vein; **f** texture of an undeformed, chloritised and partly dolomite–silica-altered basalt (transmitted light, (*tl*)); **g** plagioclase alteration in undeformed, chloritised and partly dolomite–silica-altered basalt (tl, crossed polarised (*xp*)); **h** chlorite schist close to BIF/basalt contact, crosscut by a chlorite (*chl*)–magnetite (*m*)–pyrite (*py*) vein (tl+reflected light (*rl*) and xp; **i** plagioclase (*p*)–olivine (*ol*) texture in dolerite, ol cumulates ('veinlets') in intrusion-related shear zones (tl and xp); **j** texture of olivine–plagioclase dolerite showing strong chl–dolomite (*dol*) alteration in p matrix and incipient plagioclase saussuritisation (tl); **k** spcH–q–dolomite (*d*) vein in chloritised basalt (tl)

localised appearance of coarse BIF textures suggest an isochemical rock modification (contact metamorphic overprint), probably during dike intrusions (olivine–dolerite). This will be discussed below.

Early hydrothermal magnetite–dolomite assemblage in BIF

Magnetite-2 Magnetite-2 comprises two types that are present in carbonate-altered BIF and/or iron ore. Anhedral, amalgamated magnetite-2 (anM2) is observed in carbonate-altered BIF (Fig. 10e), and euhedral magnetite-2 (euM2) in medium- to high-grade magnetite–hematite ore, which shows evidences of pre-ore carbonate alteration (Fig. 10f). Texturally indistinguishable, M1 and M2 probably represent the same growth phases. The influence of carbonate alteration on magnetite chemistry will be explored below.

Fe–dolomite-1 and Fe–dolomite-2 The earliest carbonate phase is an anhedral, granoblastic Fe–dolomite (<100 μm) that surrounds M2 (Fig. 10e). Synchronous growth with M2 in carbonate-altered magnetite BIF (Fig. 7d, f, i) is locally indicated by embayed grain boundaries between both phases. A replacement origin of dolomite after metachert

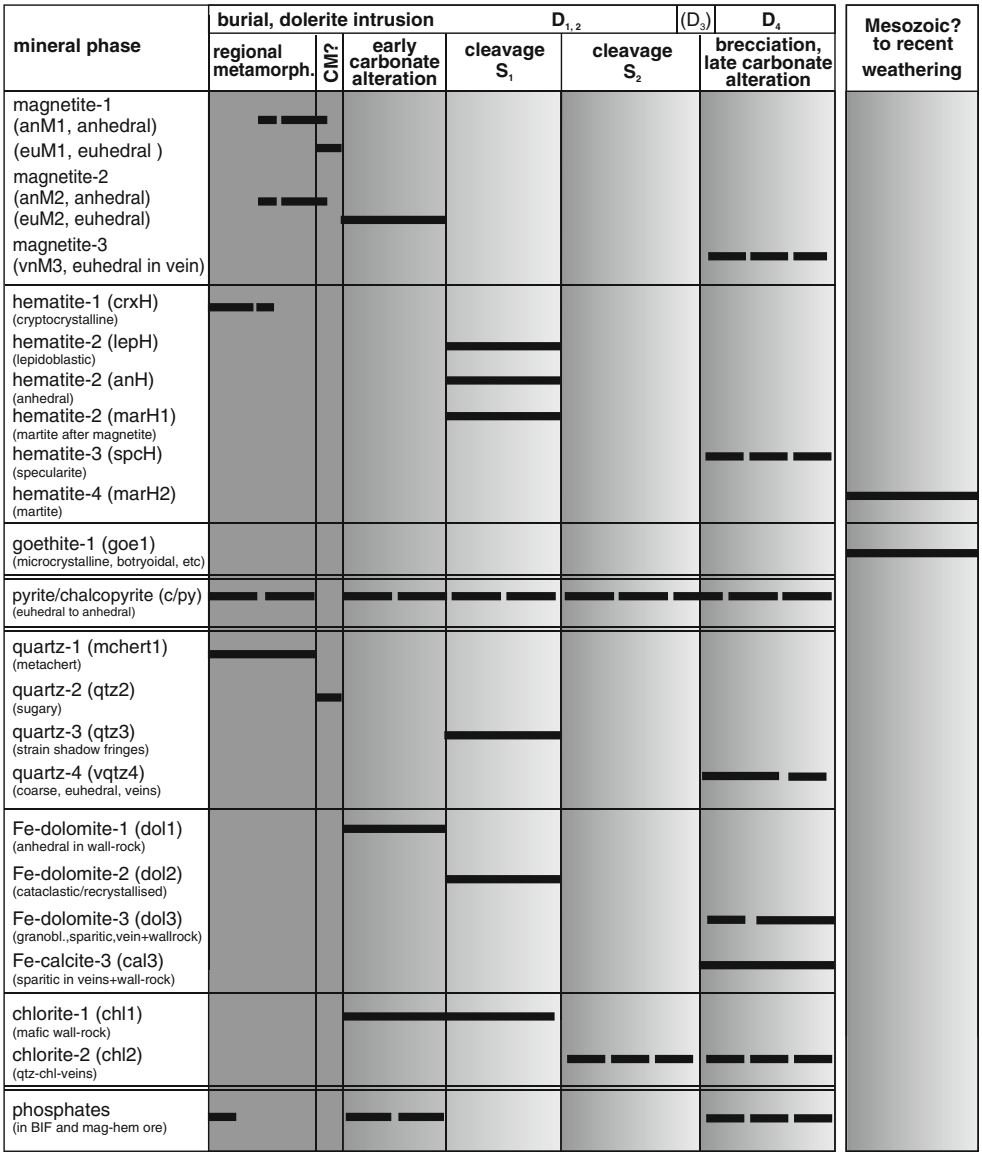

Fig. 9 Paragenetic sequence of alteration minerals and related geological events in the W2 deposit (CM?=possible contact metamorphism)

is based on hand specimen observations of alteration fronts between unaltered metachert and dolomite in the same layer (Fig. 7i) and replacement microtextures (Fig. 10g). Modifications of dolomite-1 during syn-metamorphic deformation (D_1) or static metamorphism include recrystallisation (fine recrystallised dolomite-2; Fig. 10i) and crystal annealing (sparitic dolomite-2; Fig. 7i), respectively. Chemically, they are indistinguishable (see below).

Intermediate mplH mineralisation

Microplaty, lepidoblastic and anhedral hematite Masses of randomly oriented mplH (10 to 100 μm) form hematite-rich ore (Fig. 10e) or grow as isolated grains (Fig. 10g). Two fine crystalline hematite variations are spatially related to D_1 microstructures: (1) lepH (10 to 100 μm) forms S_1 cleavages in BIF and iron ore (Figs. 5d and 10h). (2) Anhedral, granoblastic hematite (anH; 10–50 μm) define weak S_1 cleavages spatially related to euM1 in sheared BIF (Figs. 5c and 10d). In pressure fringes of euM1, anH precipitation was limited and crxH dominates (Fig. 5c). AnH grew in BIF after crxH and M1, most likely as a recrystallisation process. The lepH grew after magnetite M2 (which shows resorbed grain boundaries) and dolomite-1 and dolomite-2, also locally after M1 and metachert, to form high-grade iron ore in BIF 1 and 4 (Fig. 6). The mplH variation shows the same replacement relationships and is observed in partially mineralised carbonate-BIF in BIF 3. Hematite replaced dolomite about iso-volumetrically, without an intermediate stage of dolomite removal and porosity increase. This is evident by matrix-dominated textures devoid of any collapse (Fig. 10e, f). Dolomite removal without or limited associated hematite grow is present in laminated magnetite–martite(−hematite) ore in BIF 1 (Figs. 6a and 7f).

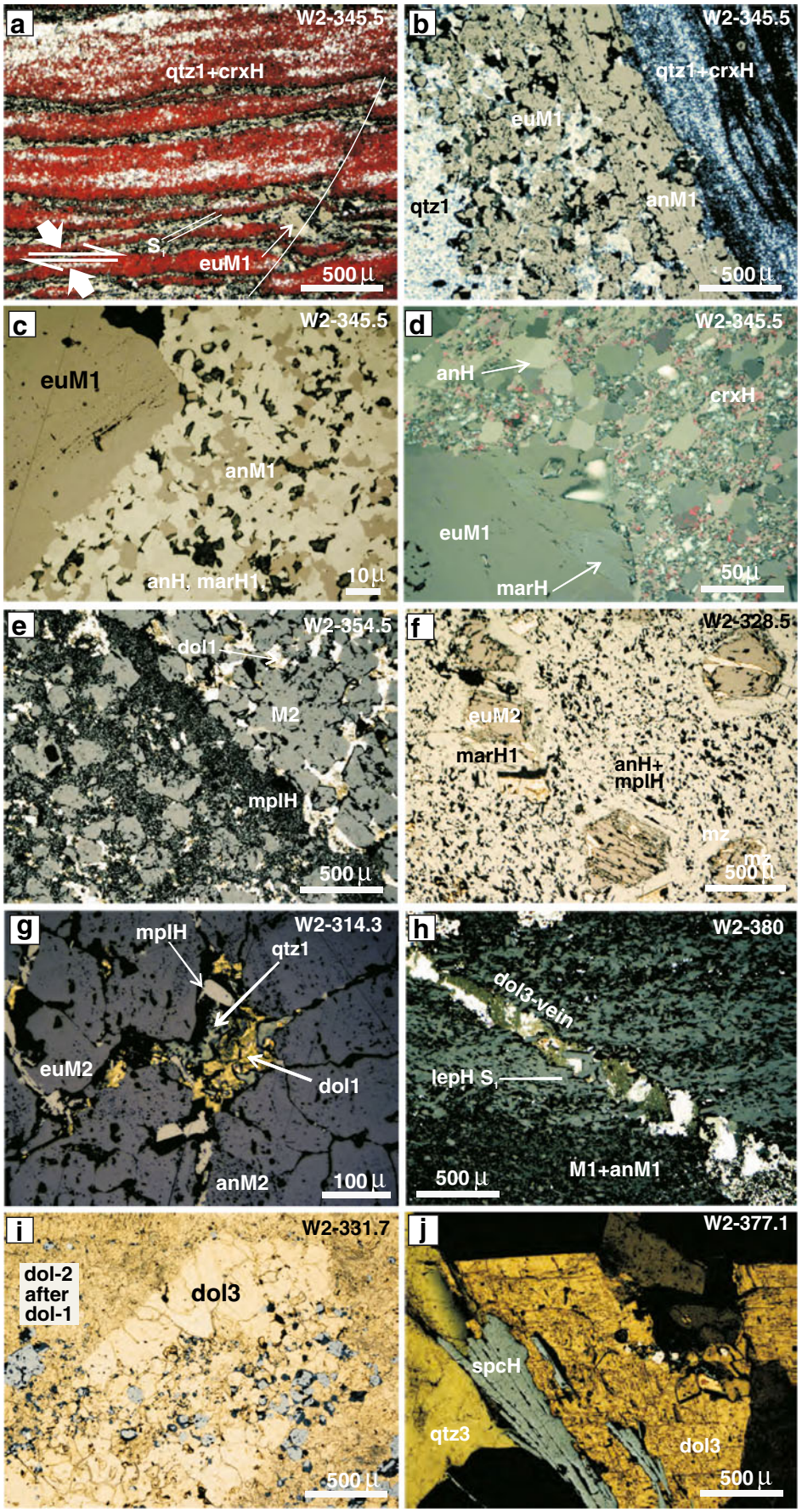

Fig. 10 Photomicrographs of thin sections showing BIF and ore types in the W2 deposit. **a** Least-altered hematite–magnetite–metachert BIF, shear fabric with rotated magnetite (*euM1*) porphyroclast (combined transmission (*tl*) and reflected light (*rl*), crossed polarised (*xp*)); **b** same sample, showing a zone of anM1+euM1 (marked as *M1*) layer (tl+rl and xp); **c** same sample, showing anhedral hematite (*anH*) having replaced anM1 and growing into porphyroblastic euM1 (rl); **d** same sample, showing early cryptocrystalline (*crxH*) being replaced by anM1 (martitised as marH) and anH (tl+rl and x); **e** medium-grade magnetite-hematite ore, in which dolomite-1 has been replaced by microplaty hematite (*mplH*; tl+rl); **f** medium-grade magnetite-hematite ore, showing euM2 in a mplH matrix with remnants of dolomite-1/2 (tl+rl); **g** carbonate-altered magnetite-BIF with remnants of primary quartz-1 and overprint of mpH (tl+rl and x); **h** fault-hosted magnetite–hematite ore with a quartz–dolomite–spcH vein (tl+rl and x); **i** carbonate-altered BIF with several overprinting stages of dolomite and magnetite (*grey*; tl+rl); **j** detail of a quartz–dolomite–spcH breccia vein (tl+rl and x)

Here, gangue layers are clearly thinned and the ore formation is associated with volume reduction of ~up to 40 % (gangue volume).

Martite-1 Below the weathering front, M1 and M2 grains are partially replaced by martite (Fig. 10d, f). This first stage of martitisation took place during the hematite alteration stage. Martite is not very common below the weathering zone, however ubiquitous within the weathering zone (martite-2, see below). This suggests that hydrothermal martitisation producing martite-1 was probably minor compared with supergene martitisation.

Quartz-3 in strain shadows Fibrous quartz-3 is observed in S_1-associated pressure fringes of magnetite porphyroblasts (Fig. 5c).

Phosphates Accessory amounts of phosphates are present in least-altered and altered BIF within and outside the deposits and can be considered as diagenetic precipitates from accessory P and rare earth element (REE; cf., Lepland et al. 2002; Nutman and Friend 2006; Bowins and Crocket 2011). The highest modal abundance of apatite, monazite and xenotime crystals is in total roughly about 0.5 vol.‰. Grains are small (10 to 100 μm), serrate and intergrown with iron oxides in magnetite–hematite fault-breccias that crosscut BIF 4. Based on studies conducted on hematite-rich iron ore in the Hamersley Province (Rasmussen et al. 2007), these phosphates are hydrothermal in origin and are potential geochronometers for hydrothermal hematite mineralisation.

Late hematite–dolomite–quartz vein alteration

Specular hematite Coarsely crystalline hematite (spcH; millimetres to several centimetres in size) is present, together with quartz±dolomite, in pods in dolomite-altered BIF and/or high-grade iron ore (Fig. 7d). The spcH blades are unstrained and mineral inclusion poor (Fig. 10j). Fine-grained types of spcH are present in thin veins crosscutting BIF and magnetite–hematite ore.

Quartz-3 Locally, large euhedral quartz (>mm), often associated with spcH in pods or in carbonate-altered BIF, replaced carbonate-1 or carbonate-2 (prismatic ghost shape in Fig. 10i). Quartz in granoblastic and undeformed veins may be related to the same quartz-3 generation.

Fe–dolomite-3 Locally, undeformed granoblastic or sparitic Fe–dolomite (dolomite-3) veins and breccia pods crosscut BIF and magnetite–hematite ore (Figs. 7e, k and 10h). Dolomite-3 replaced locally euhedral quartz-3 (Fig. 10i) and dolomite veins often truncate quartz veins, but many veins show quartz and dolomite in equilibrium (Fig. 10k).

Chlorite, magnetite-3 and pyrite Close to mafic wall rocks, chlorite±pyrite replacing dolomite-1/2 is commonly observed in BIF and ore. Euhedral magnetite-3 in veins (vnM3) is in equilibrium with carbonate-3. The vnM3 is a prominent rock alteration in the <1-m thick, high-grade magnetite±pyrite±chalcopyrite zones at the contact with mafic rocks (Fig. 6).

Supergene assemblages in BIF and ore

Martite-2 and goethite Martite and goethite commonly replace carbonate, quartz and all magnetite in the weathering zone. Outcrop relationships observed in the W2 open pit suggest that goethite in meter-scale halos surrounding high-grade goethite–hematite–martite ore are in many places spatially associated with spcH-rich veins or pods (Fig. 7k).

Whole-rock geochemistry

Eighteen samples from drill core W2DDH007 and the W2 open pit have been selected for whole-rock geochemistry, including XRF (major element oxides), ICP-MS (trace elements), S, C (both with LECO combustion method) and ferrous iron determination (by titration). Representative samples of the following lithology/alteration groups are analysed: quartz–hematite–magnetite BIF (least-altered, two samples from BIF 3), weakly carbonate-altered BIF (three samples from BIF 4), carbonate-altered BIF (two from BIF 2 and one from BIF 3), one fine-grained magnetite–hematite ore (from BIF 3 and 4) and one coarse-grained goethite–martite (from BIF 3). Geochemical data from the quartz–magnetite BIF from the Koolyanobbing K deposit are included (Angerer et al. 2012) as a reference for least-altered BIF in the lower greenstone succession of the Southern Cross domain, Yilgarn Craton.

Analytical methodology

Whole-rock samples (300 to 500 g each) were coarsely crushed in a steel jaw crusher and then milled to a powder (<100 μm) in a Cr-steel mill (leading to contamination of Cr and minor Fe), with ‘silica glass washes’ in between. About 30 g of the homogenised powder were analyzed at ACME laboratory in Vancouver, Canada by means of XRF (ten major oxides) and ICP-MS (45 trace elements). For the XRF, a Li borate fusion was used and for the ICP-MS a Li borate fusion followed by nitric acid digestion and a

separate Aqua Regia digestion to analyse precious and base metals. Loss on ignition (LOI) at 1,000 °C was determined gravimetrically, total sulphur and carbon by LECO© combustion analyses and ferrous iron by volume titration following acid digestion.

Analytical accuracy was tested with the international geochemical BIF standard FeR-3 from Temagami, Canada (Bau and Alexander 2009). Precision was tested with blind duplicates. Results of both tests are summarised in Angerer et al. (2012).

An Fe^{2+} number for BIF and ore samples is calculated from cations by $Fe^{2+}/(Fe^{2+}+Fe^{3+})$. All discussed REE fractionation trends are based on chondrite normalisation after Sun and McDonough (1989) and on PAAS normalisation after McLennan (1989). The Ce and Eu anomalies, normalised to chondrite, are calculated $(Ce/Ce^*)_{CN}=Ce/(La\times Pr)^{0.5}$ and $(Eu/Eu^*)_{CN}=Eu/(Sm\times Gd)^{0.5}$, respectively. Following Alibo and Nozaki (1999) and Alexander et al. (2008), PAAS-normalised La, Gd and Pr anomalies are calculated: $(La/La^*)_{PAAS}=La/(3Pr-2Nd)$, $(Gd/Gd^*)_{PAAS}=Gd/(0.67Sm+0.33Tb)$ and $(Pr/Pr^*)_{PAAS}=2Pr/(3Nd-Sm)$, respectively. The data of the whole-rock, trace and REE analyses and calculated ratios are presented in the Electronic supplementary material (ESM).

Major element (oxides)

Least-altered quartz–hematite–magnetite BIF Two least-altered BIF samples in BIF 3 are rich in SiO_2, Fe_2O_3 and FeO*. Minor amounts (0.2 to 2 wt.%) of CaO, MgO and C and trace amounts (<0.2 wt.%) of Al_2O_3, MnO, P_2O_5 and S are present (Fig. 11a). The major element content of BIF at Windarling is compatible with average BIF chemistry from the Yilgarn Craton (Gole 1981).

Carbonate-altered BIF Compared with least-altered BIF, the low concentrations of SiO_2 (<1 wt.%, Fig. 12a) and high concentrations of MnO, CaO and MgO (~0.4, 6–8 and >10 wt.%, respectively) in carbonate-altered BIF samples are the results of almost complete replacement of silica by carbonate (Figs. 13a and 12c, d). The weakly carbonate altered samples show similar trends but they are less pronounced. The P_2O_5 values in all carbonate-altered BIF samples are significantly higher in carbonate- and weakly

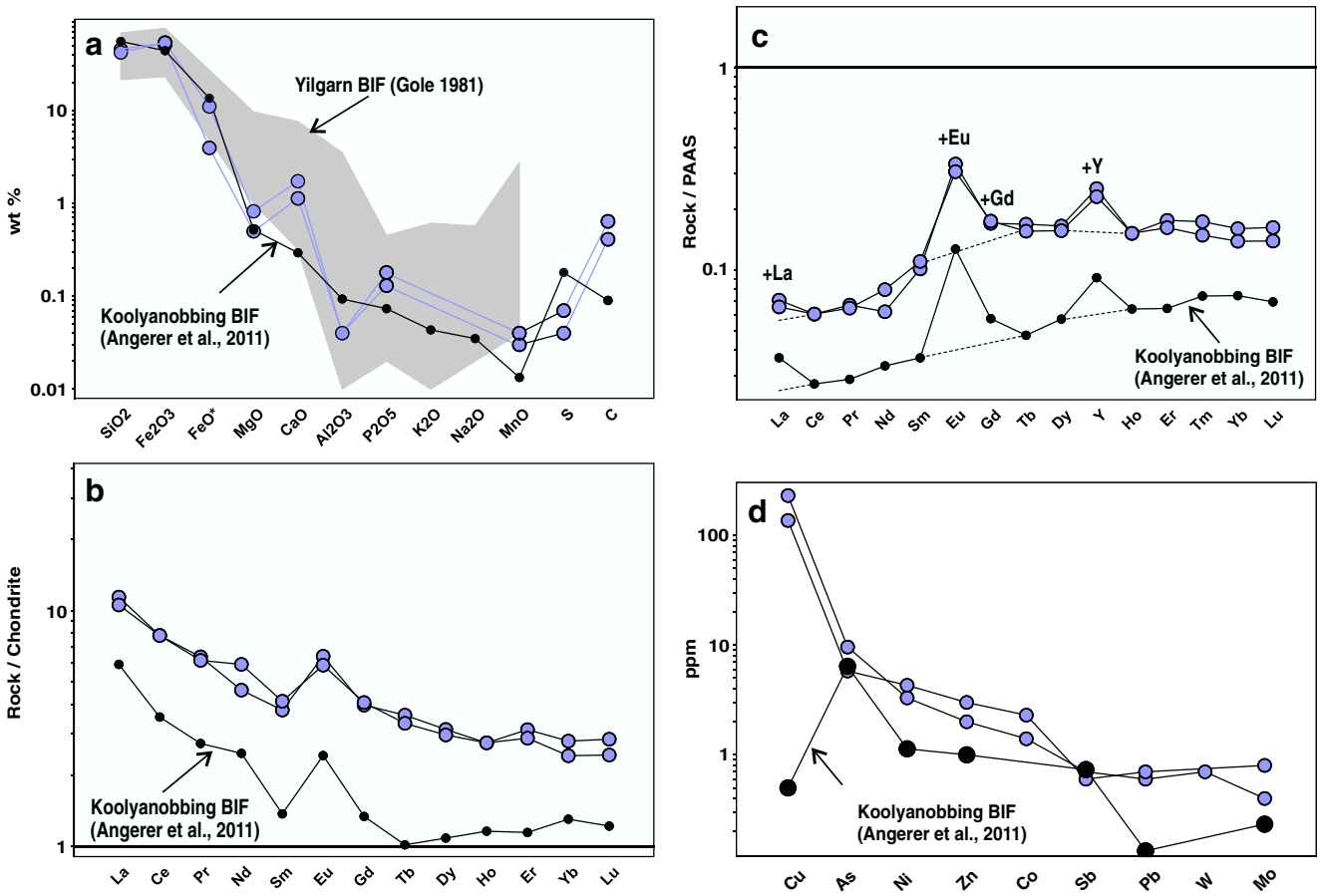

Fig. 11 Whole-rock geochemistry. **a** Major oxides, **b** REE chondrite normalised (Sun and McDonough 1989), **c** PAAS normalised (McLennan 1989) and **d** trace metals in least-altered BIF. Shown in *shaded areas* are also Koolyanobbing least-altered and average Yilgarn BIF

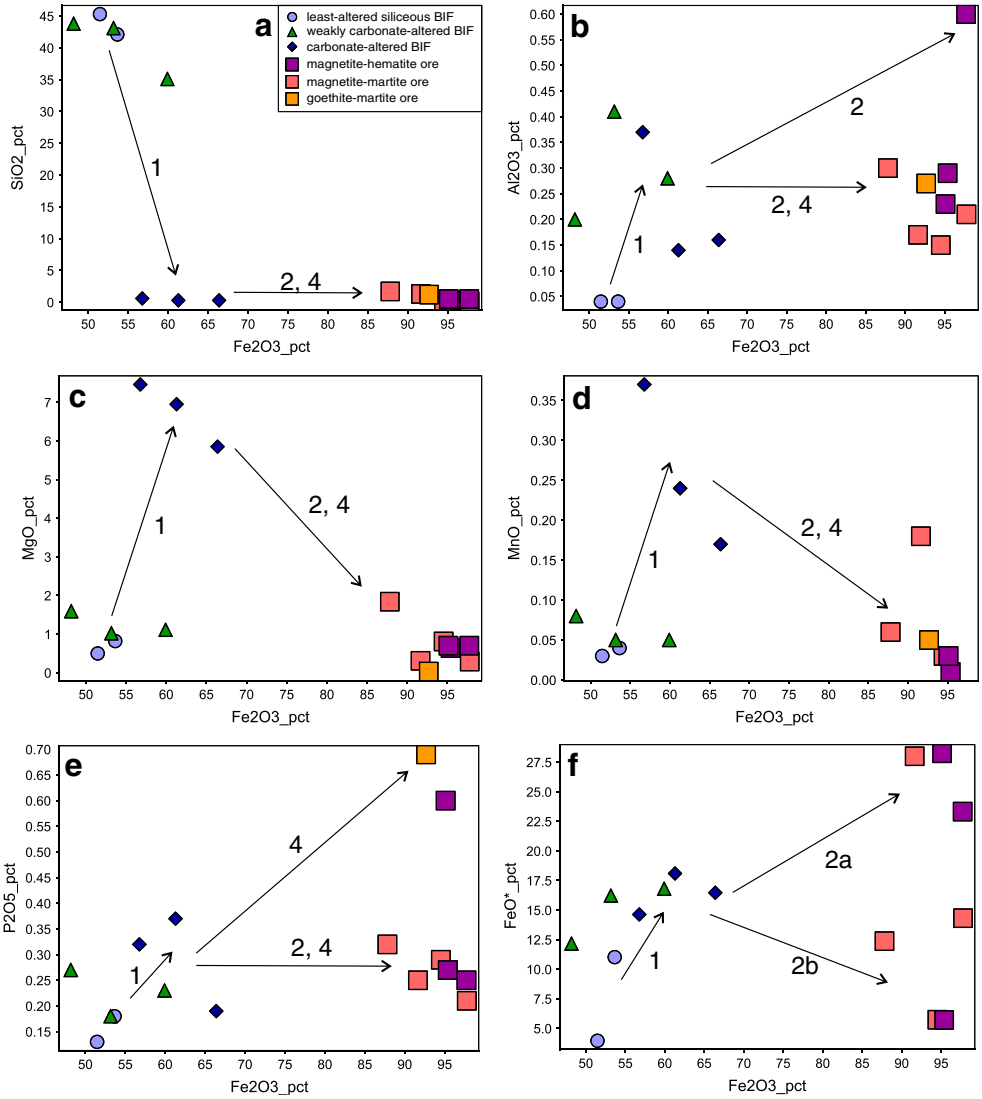

Fig. 12 Whole-rock geochemistry—binary plots showing Fe_2O_3 versus major oxides of W2DDH007 samples —**a** SiO_2, **b** Al_2O_3, **c** MgO, **d** MnO, **e** P_2O_5 and **f** FeO* (i.e. ferrous iron)

carbonate-altered BIF (Fig. 12e). The high ferrous iron content in carbonate-altered samples (Fig. 12f) is a result of the progressed transformation of crxH to magnetite.

Magnetite–hematite(−martite) ore The Fe_2O_3 content in magnetite–hematite(−martite) ore is >83 wt.%, indicating that hypogene iron ore is below the present weathering front at W2 (Fig. 13b). Silica concentrations are very low (0.01 to 0.2 wt.%) when compared with least-altered BIF, but further loss during ore formation is minimal, considering that most silica has already been replaced during carbonate alteration, which represents a proto-ore stage genetically associated with the iron ore (Fig. 12a). The ferrous iron content is strongly variable. Lower values (<10 wt.%) are comparable with hematite-bearing, least-altered BIF and broadly correlates with the magnetite/hematite ratio (Fig. 12f).

Goethite–martite ore Goethite-dominated ore is strongly depleted in MgO, CaO, MnO, K_2O and Na_2O (Fig. 13b), when compared with BIF. Ferrous iron was not analysed but can be considered to be a minor constituent due to strong oxidation associated with supergene alteration. Phosphorous is enriched in goethite–martite ore of BIF 3, compared with all other lithologies (Fig. 12e). The SiO_2 and Al_2O_3 values are in the range of those from hypogene-zone magnetite–hematite ore samples.

Trace elements and REE

Least-altered quartz–magnetite BIF Transition metals are, except for Cu (100–200 ppm), below 10 ppm in BIF (As> Ni>Zn>Co>Sb, Pb, W and Mo; Fig. 11d). Average REE concentration in BIF is 14 ppm. An Archean BIF-typical fractionation trend with high positive La, Eu, Gd and Y anomalies and flat HREE (Bau and Möller 1993; Ohmoto et al. 2006) is observed (Fig. 11b, c).

Carbonate-altered BIF Almost all trace elements are enriched in carbonate-altered BIF (Fig. 13e) when compared

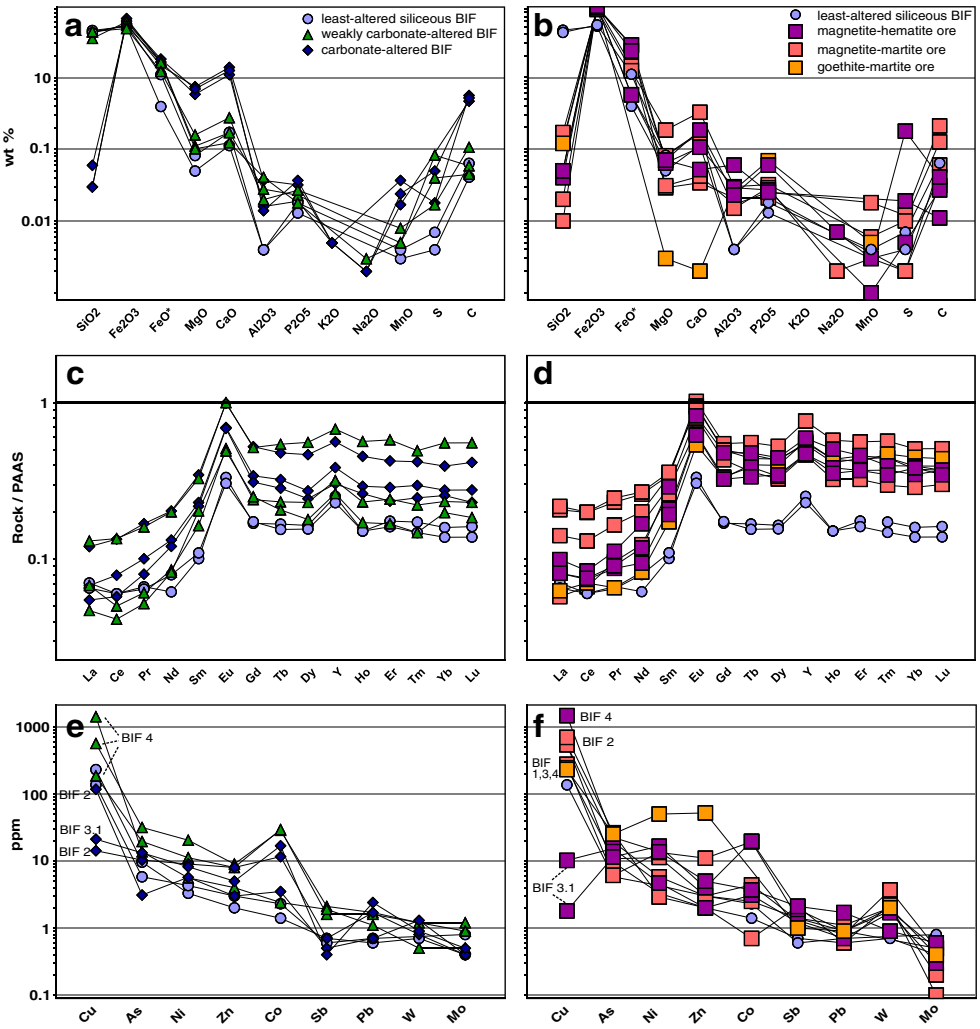

Fig. 13 Whole-rock geochemistry plots. Major oxides in *upper row*, REE in *middle row* and trace metals in *lower row* of (**a**, **c**, **e**) carbonate-altered BIF and (**b**, **d**, **f**) high-grade ore. As a reference the least-altered BIF are plotted as well (*light blue circles*)

with least-altered BIF, but the weakly carbonate-altered BIF in BIF 4 has a generally higher content of Mo, Cu, Zn, Ni, As and Sb, independent of the intensity of the hydrothermal alteration. This suggests variations in the primary sedimentary facies of the individual BIF units. In the majority of carbonate-altered samples, the Co content is anomalously high (>10 ppm), compared with least-altered BIF (<1 ppm). The ΣREE increases roughly with the intensity of carbonate and/or phosphate alteration (Fig. 13c).

Magnetite–hematite (martite) and goethite–martite ore Trace metals content in ore types are similar to carbonate-altered BIF (Fig. 13f), showing a generally high Cu (not in all samples) and locally high Co content in magnetite–hematite and magnetite–martite ore. Molybdenum is depleted in all ore samples when compared with BIF.

Magnetite-rich (hypogene hydrothermal ore) and martite–goethite (supergene-modified) ore show higher ΣREE than BIF but similar fractionation trends (Fig. 13d). Variations are present in magnetite–hematite and in martite–goethite ore MREE and HREE are much stronger enriched than LREE. This is not the case in magnetite–martite ore, where the enrichment is the same in all REE. In all ore types, specific element anomalies (La, Eu, Gd and Y) are retained.

Mineral trace-element geochemistry

Five samples that are representative of the various types and generations of magnetite, hematite, Fe–dolomite and phosphates, which occur in least-altered BIF (W2-345.5), carbonate-altered BIF (W2-331.7 and W2-343.4) and magnetite–hematite ore (W2-377.1 and W2-380.8), have been analysed using in situ Laser Ablation ICP-MS in order to obtain trace element concentrations. In addition, Fe–dolomites and phosphates have been analysed for major elements by SEM-EDX. Results from the Koolyanobbing K deposit iron oxides, reported in Angerer et al. (2012), are shown for comparison.

The generally very low trace elements and REE contents in iron oxides (e.g. Figueiredo e Silva et al. 2009;

Nadoll et al. 2009; Angerer et al. 2012) require low detection limits, which presently can only be achieved by laser ablation ICP-MS. Analytical methodology is the same as described in Angerer et al. (2012). STDGL2b-2 (Danyushevsky et al. 2003) was used as a primary standard to calculate concentrations of oxides and to correct for instrument drift. The international standard glass NIST612 was used as carbonates. Matrix correction for dolomite was achieved by SEM-EDS quantification of Ca, and for magnetite and hematite, stoichiometric Fe content was assumed. Data tables including average limits of detection are available as ESM.

Magnetite

The metamorphic magnetite types, anM1 and euM1, have indistinguishable chemistry (Fig. 14a), suggesting isochemical growth of euM1 after anM1 and, therefore, support a common genesis. Minor and trace elements are Mg (100–600 ppm), Al (60–150 ppm), Mn (30–50 ppm) and Ni, Zn, Co, Ti, V and Ga (1–9 ppm).

The anM2 in carbonate-altered BIF is chemically very similar to M1 (Fig. 14b), except elevated Mn and Ti values. On the other hand, euM2 in high-grade ore associated to carbonate alteration shows lower Mg, Al and Zn and higher Ni and Co (and V, Ti?), when compared with the other magnetite species. The Mg content in carbonate BIF-hosted M2 is not higher than in siliceous BIF-hosted M1, ruling out significant effects of dolomite inclusions in magnetite to the chemistry.

Hematite

Hydrothermal martite has a similar chemistry to its magnetite precursor euM1 and anM2 (Fig. 14c, d), except Ti, which is contentiously enriched. Anh and lepH chemistries are distinct to magnetite, showing generally lower Co, Ni, Zn, Mn, Mg and Ga and higher V, Ti and Al concentrations (Fig. 14e). Comparing coarse spcH from a spcH–Fe–dolomite–quartz pod and a fine spcH from a vein in carbonate-altered BIF with lepH, the similarity of most element contents (Al, Ti, V, Pb, W, Ga and Y) is evident (Fig. 14f).

Dolomite

Fine Fe–dolomite-1/-2 and sparitic dolomite-3 have been analysed in the various alteration zones. All dolomite types are characterised by similar Fe and Mn substitution for Mg in the lattice (Fig. 15a); the fine-grained dolomite has highly

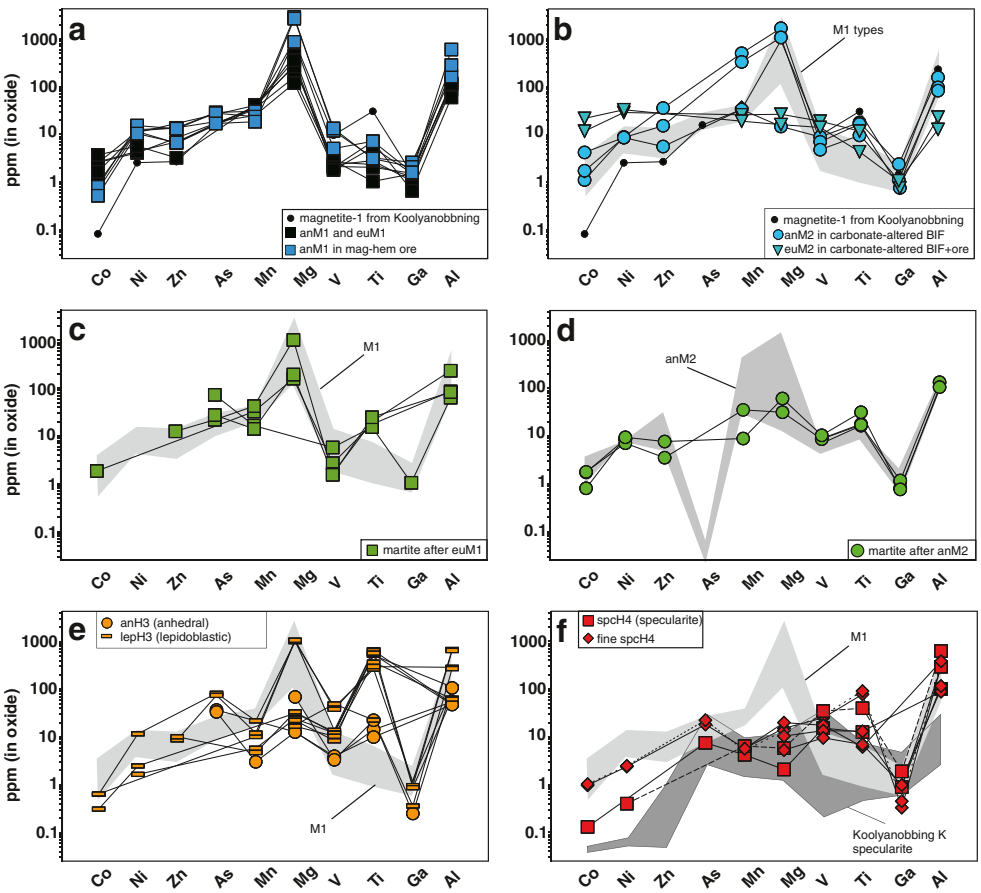

Fig. 14 Iron oxides chemistry (elements compatible in the 'spinel' structure: Mg, Al, Mn, Ti, V, Ga, Zn, Ni and Co) of selected samples from drill core W2DDH007. **a** Metamorphic magnetite (M1 types) in Windarling W2 deposits, together with magnetite-1 from Koolyanobbing for comparison; **b** anM1 core in euM2 from a carbonate-altered BIF, together with anM2 in carbonate-altered BIF and euM2 in magnetite–hematite ore; **c** martite after anM1a, compared with M1 types (*grey area*) shows the changes in chemistry related to martitisation; **d** martite after anM2 (*grey area*); **e** anH and lepH with *grey area* representing M1-types magnetite; **f** spcH types with *dark grey area* showing Koolyanobbing K deposit spcH and *light grey area* representing M1-type magnetite

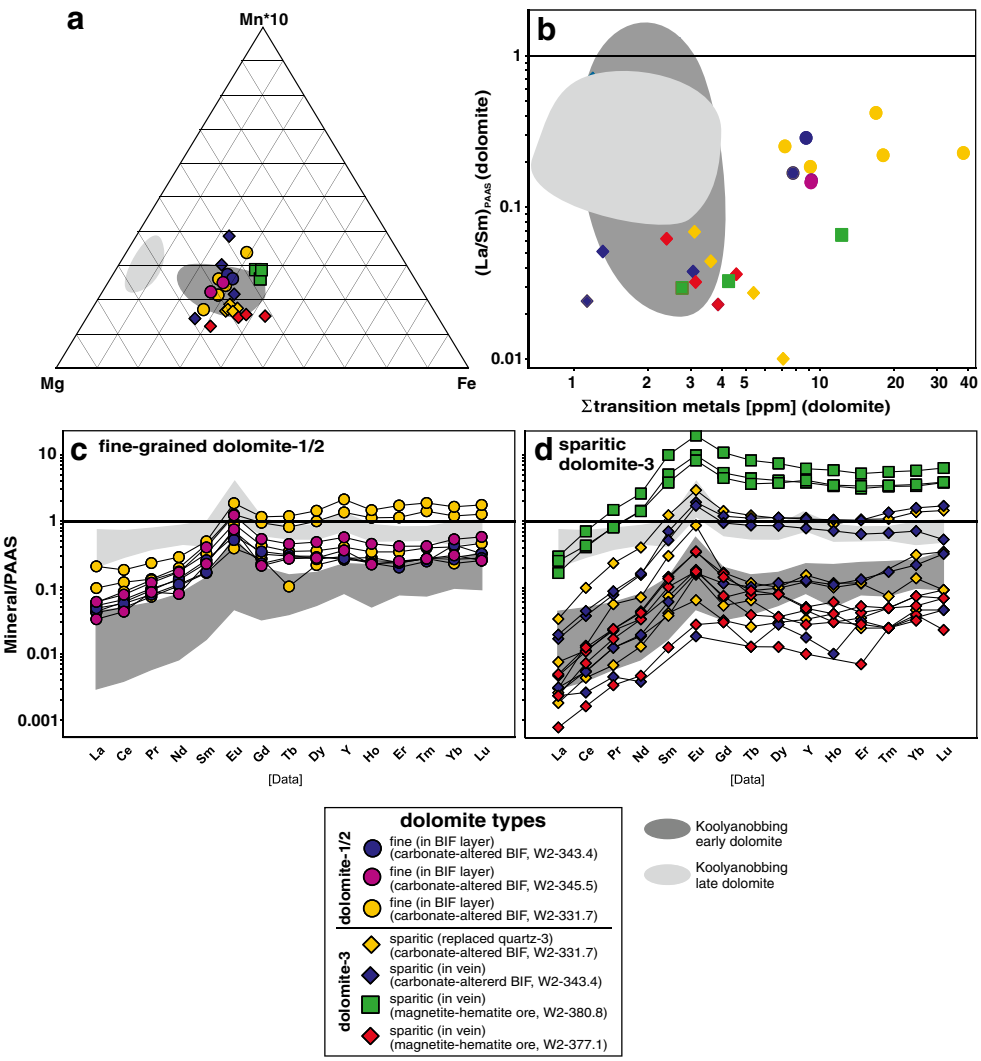

Fig. 15 Fe–dolomites chemistry (dolomite 1/2—early, fine-grained stages and dolomite 3—late, sparitic stage) of selected samples from drill core W2DDH007. **a** Ternary Fe–Mg–Mn*10 diagram displaying a similar major chemistry of all dolomite stages; **b** total transition metal concentration (Ni+Co+Cu+Zn) versus PAAS-normalised LREE fractionation plot differentiates between early and late stages in Windarling; **c** PAAS-normalised REE diagram with early dolomite stages compared with Koolyanobbing, showing a narrow range of REE content; **d** PAAS-normalised REE diagram with late dolomite stage, shows a wide range of REE concentration. *Grey areas* displaying early (*dark*) and late (*light*) dolomites from Koolyanobbing for comparison

variable MnO (0–2.4 wt.%) and FeO (0.5–9.5 wt.%) contents, whereas the sparitic dolomite shows a relatively narrow Fe+Mn signature (FeO, 6.5–10 wt.%; MnO, 0.5–0.8 wt.%). The transition metal content is high in dolomite-1 and dolomite-2 (>7 ppm) and low in sparitic dolomite-3 (<7 ppm with one outlier at 14 ppm) (Fig. 15b). Significant differences between fine and sparitic Fe–dolomite are evident in the REE pattern: sparitic dolomite-3 shows stronger LREE fractionation (smaller $(La/Sm)_{PAAS}$ ratios), compared with dolomite-1 and dolomite-2 (Fig. 15b). Both types have a distinct positive Eu anomaly (Fig. 15c, d). The ΣREE are highly variable in sparitic dolomite (<1 to 200 ppm).

Descriptive mineralisation and structural model for the Windarling iron ore deposits

A descriptive mineralisation and structural model for the Windarling deposits is based on detailed pit mapping, core logging, petrographical, geochemical and mineral chemical analyses. The key geochemical processes that took place during BIF genesis and ore forming stages are summarised as sketches in Fig. 16. Analyses of the trace element and REE element patterns of least altered BIF to high-grade ore stages including the BIF and hydrothermal alteration stages, allows preliminary constraints on the fluid chemistry during the evolution of the Windarling BIF-related iron ore system. A hydrothermal fluid analysis with stable isotopes and fluid inclusions is presently in progress.

Seafloor alteration in mafic rocks and BIF deposition

Hydrothermal alteration in the basalts is polyphase, beginning with seafloor alteration (cf., Dalstra et al. 1999). For the Windarling Range basalts, this early alteration is inferred, based on strong saussuritisation of plagioclase. The dolerite sill, on the other hand, is devoid of these alterations and therefore it resembles an intrusion that most likely postdates seafloor alteration. Basalts and dolerite show alteration

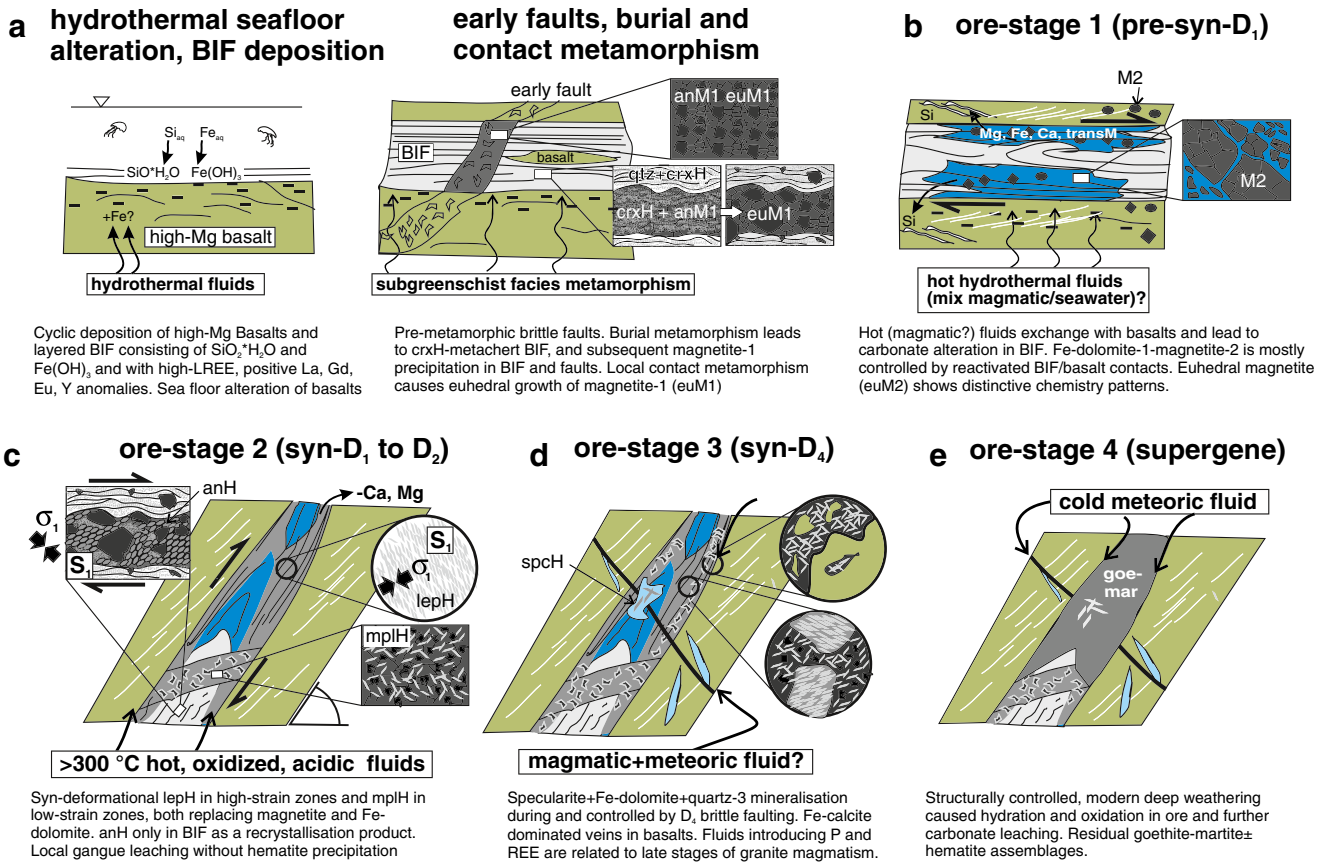

Fig. 16 Geological evolution and ore forming stages of the Windarling W2 deposit

associated with a later hydrothermal alteration stage, which is characterised by chlorite growth replacing primary Mg–Fe–silicates. A penetrative chlorite cleavage is developed in the basalts proximal to BIF/ore boundaries. BIF precipitated cyclically in times of volcanic quiescence forming the regional- to local-scale interlayered volcano-sedimentary stratigraphy typical for the Windarling Range (Fig. 16a). Iron precipitated as $Fe(OH)_3$, formed either by photosynthesis or photooxidation of Fe^{2+} from hydrothermal solutions in the ocean (Eq. 1 in Table 2; Bekker et al. 2010, and references within). The PAAS-normalised La, Eu, Gd and Y anomalies in all BIF units (Fig. 11c) are typical for Archean BIF and supports the signature of hydrothermally fertilised seawater (Dymek and Klein 1988; Danielson et al. 1992; Bau and Möller 1993; Bau and Dulski 1996, 1999; Ohmoto et al. 2006; Bolhar and Van Kranendonk 2007; Planavsky et al. 2010).

Very-low-temperature regional burial metamorphism and local contact metamorphism

A sub-greenschist facies peak metamorphism across the Windarling Range is indicated by predominantly incipiently recrystallised (metacherty) quartz in least-altered BIF. This burial metamorphism recorded in BIF is supported by paleotemperature estimations based on oxygen isotopic equilibrium between quartz and magnetite (*unpublished data*) and are compatible to regional P/T estimates for BIF in the Marda greenstone belt (Dalstra et al. 1999). During burial metamorphism, crxH formed by dehydration of $FeOH_3$ (Eq. 2a in Table 2), and successively M1 by crxH reduction (equation 2b), both representing the metamorphic iron oxide types (Fig. 16a). Co-existing crxH and M1 represents non-equilibrium metamorphic conditions. This is similar to 'jaspilites' from the Carajas region in Brazil (Figueiredo e Silva et al. 2008), where the dominant iron oxide crxH is also described as the paragenetic earliest (preserved) iron oxide.

A genetic and temporal differentiation between regional burial metamorphism and local (contact metamorphic) coarsening of BIF is equivocal; the chemical similarity between anM1 and euM1 (Fig. 14a) indicate that both magnetite types are genetically linked. It is speculated here that the dolerite sills were the heat source for local isochemical coarsening of BIF, although a clear spatial correlation is not evident. Contact metamorphism did not involve metamorphic silicate formation, probably due to low fluid–rock ratio and low cation content in solution.

Table 2 Important mineral assemblages, chemical reactions and reaction conditions for ore-forming stages in the Windarling W2 deposit

Equation	Key chemical reaction(s)	BIF- and ore-forming stage	Key mineral assemblage	Conditions of fluid-rock interaction
1	$2Fe^{2+}_{aq} + 0.5O_2 + 5H_2O \rightarrow 2Fe(OH)_3 + 4H^{+}_{aq}$[a] and $SiO_{2aq} \rightarrow SiO_{2s}$	BIF deposition	$Fe(OH)_3$+SiO_2 (reciprocal concentration and microband interlayered)	Photosynthesis or photooxidation of Fe^{2+} from hydrothermal solutions in the Archean ocean
2a 2b	$2Fe(OH)_3 \rightarrow Fe_2O_3 - 3H_2O$ followed by $3Fe_2O_3 \rightarrow 2Fe_3O_4 + 0.5O_{2aq}$ (and quartz mobilisation/precipitation)	BIF regional and local contact metamorphism	crxH+metachert followed by magnetite-1+metachert	Prograde very-low grade metamorphism with dehydration (hematite formation) followed by magnetite reducing replacement
3	$Fe_2O_3 + 1.2Fe^{2+}_{aq} + 0.8Mg^{2+}_{aq} + Ca^{2+}_{aq} + 2CO_3{}^{2-}_{aq} + 2OH^{-}_{aq} \rightarrow Fe_3O_4 + (0.2Fe,\ 0.8Mg)Ca(CO_3)_2 + H_2O$ (and quartz mobilisation)	1 (pre- to syn-D1)	Magnetite-2+Fe–dolomite	Metal-rich, reduced, basic brine(?) interacts with BIF, dolomite+ magnetite replace crxH
4	$Fe_3O_4 + (0.2Fe, 0.8Mg)Ca(CO_3)_2 + 2H^{+}_{aq} \rightarrow Fe_2O_3 + 1.2Fe^{2+}_{aq} + 0.8Mg^{2+}_{aq} + Ca^{2+}_{aq} + 2CO_3{}^{2-}_{aq} + H_2O$ (and quartz mobilisation)	2 (syn-D1 or -D2)	mplH+lepH+anH–Fe–dolomite	(Pressure accommodated) hematite replacement and dolomite dissolution under weakly acidic and oxidised conditions
5	$Fe_3O_4 + 4Mg^{2+}_{aq} + 5Ca^{2+}_{aq} + 10CO_3{}^{-}_{aq} + 2H^{+}_{aq} \rightarrow Fe_2O_3 + 5(0.2Fe, 0.8Mg)Ca(CO_3)_2 + H_2O$ (and quartz mobilisation/precipitation)	3 (syn-D4)	spcH+Fe-dolomite (+quartz)	spcH–dolomite–quartz vein assemblage forms under hydrous, oxidising conditions by consuming existing magnetite, dolomite and quartz
6	$Fe_3O_4 + 2(H_2O) \rightarrow 3FeOOH + H+_{aq}$ (and dolomite and quartz mobilisation)	4 (supergene)	Goethite	Hydrous oxidation
7a 7b	$2Fe_3O_4 + 0.5O_{2aq} \rightarrow 3Fe_2O_3$ or $Fe_3O_4 + 2H^{+}_{aq} \rightarrow Fe_2O_3 + Fe^{2+}_{aq} + H_2O$[b]	Martite formation during ore stages 2, 3 and 4	marH after magnetite (pseudopmorphism)	Hydrous oxidation or non-redox[b]

For mineral abbreviations, see Fig. 9, i.e. paragenetic sequence

[a] Bekker et al. (2010)

[b] After Ohmoto (2003)

Ore stage 1: early carbonate alteration during a Fe+Ca+Mg +Ni+P metasomatic event

Evidence for early metasomatism in BIF surrounding iron ore includes localised growth of dolomite-1 and magnetite-2. Recrystallisation of fine dolomite-2 and intense ductile deformation in carbonate-altered BIF, when compared with quartz-rich BIF (Fig. 7c), suggest that early dolomite alteration took place prior to ductile D_{1b} and D_2 deformation. Brittle D_{1b} structures that controlled fluid flow during ore stage 1, such as BIF-crosscutting faults (see BIF 4 in Fig. 6b) and reactivated BIF-basalt margins (e.g. BIF 2 in Fig. 6a), formed at a shallow crustal level during the early stage of orogenesis (basin inversion?). The BIF units' small thickness of 10 to 20 m allowed locally a complete replacement of chert bands (in BIF 1 in Fig. 6a). All these sites were subject to subsequent partial to complete magnetite–hematite±pyrite ore formation.

The ubiquitous lack of crxH in carbonate-altered rocks and related magnetite–hematite ore is a result of replacement of hematite by magnetite under fluid-rock conditions that were likely somewhat reduced, based on the stability of magnetite under lower oxygen fugacity, compared with hematite. The variable magnetite-2 chemistry patterns (Fig. 14b) show both, a close relationship of anM2 to M1 and a distinct fluid-derived chemistry in euM2. This suggests a generally common pre-carbonate alteration genesis of anM1 and anM2 but also a significant chemistry control of the hydrothermal carbonate-introducing fluid on the euM2 chemistry.

Although overall similar trace element patterns provide evidence for a common origin of least- and carbonate-altered BIF (Fig. 13c, e), their major element chemistry is profoundly different (Figs. 12a and 13). The metasomatic carbonate-rich hydrothermal fluids was silica undersaturated, presumably reduced and basic, rich in CO_3^{2-}, Fe, Mg, Ca, Mn, S and P providing favourable fluid–rock conditions for the precipitation of Fe–dolomite, phosphates and minor sulphides and the dissolution of SiO2, but unfavourable for silicate formation (Eq. 3 in Table 2). In addition, significant enrichment of Zn, Co and Ni took place during carbonate alteration (Fig. 13e), which is also reflected in high transition metal content in euM2, when compared with M1 and anM2 (Fig. 14b) and in early-stage dolomite-1, when compared with late-stage dolomite-3 (Fig. 15b). The proposed isovolumetric replacement of metachert by denser Fe–dolomite implies a mass increase in the BIF.

The fluids of the hydrothermal ore stage 1 show chemical characteristics resembling the typical chemistry of mafic rocks. Considering the strong alteration of the country rock basalt, it is likely that hydrothermal fluids interacted with basalts, i.e. scavenging elements and becoming more reduced, prior to reacting with the BIF (cf., Angerer et al. 2012). At the BIF-hydrothermal fluid interface the chemical potential between BIF and fluid led to dissolution of quartz and precipitation of a dolomite–magnetite±phosphate±sulphide assemblage.

Ore stage 2: deformation-controlled hematite mineralisation and gangue removal

Ore stage 2 involved several processes: (1) ductile deformation in BIF and recrystallisation of dolomite-1 to dolomite-2 during the late north–south compressional D_1 and/or D_2 event, (2) dissolution of dolomite (Fig. 16c), (3) hematite formation (mplH and lepH) preferentially after dolomite and magnetite, and limited anH after crxH, magnetite and quartz and (4) martitisation. The recrystallisation of dolomite-1 in ductile deformed carbonate-altered BIF was associated with a high fluid-rock ratio and took place at temperatures probably around or above 270 °C (minimum temperature for dolomite recrystallisation under wet conditions, cf., Newman and Mitra 1994). Hematite replaced M1 and M2, early Fe–dolomite and quartz, as suggested by chemical Eq. 4 in Table 2. This reaction is principally the reverse one to ore stage 1 but now under oxidative and acidic conditions. Martitisation by oxidation or non-redox transformation under acidic conditions (Ohmoto 2003) of magnetite (chemical Eq. 7a, b, respectively, in Table 2) accompanied ore stage 2. Presence of dissolved H^+ in the fluid–rock system may have accommodated both processes. The lack of significant cation exchange during hydrothermal martitisation of M1 and anM2 (Fig. 14c, d) supports the oxidation reaction, as this is devoid of Fe^{2+} (and associated cations) mobilisation (Table 2). In addition, an estimated volume decrease of 32 % (Mücke and Raphael Cabral 2005) during non-redox reaction is not compatible with the observations of near iso-volumetric and non-porous martitisation (Fig. 10d, f)

Undeformed mplH formed in several zones in the BIF units, for example in crosscutting faults and along BIF-basalt margins. In sheared zones, however, lepH cleavages (S_1) were generated forming a schistose high-grade iron ore. Therefore, in the W2 deposit, lepH mineralisation is a deformation-controlled ore upgrade process. The D_1-flexural slip-folded BIF that lack carbonate alteration was a preferred site for anhedral granoblastic hematite replacing crxH by recrystallisation and M1. This replacement process did not upgrade BIF with respect to the iron content. Mineral chemistry depicts the distinct genesis of anH and lepH: it is evident that in lepH most cations generally display a higher concentration (Fig. 14e), suggesting that the hydrothermal fluid, from which lepH precipitated, was cation-enriched after magnetite and dolomite-1 dissolution. An order of magnitude higher Ti contents (up to 676 ppm), compared with hydrothermal hematite, suggest that Ti was mobile at least during ore stage 3.

Dolomite displacement during ore stage 2 devoid in hematite precipitation formed texturally thinned, laminated magnetite±hematite ore (Fig. 7e) with minor additional hematite precipitation. Generally, carbonate solubility increases with confining pressure and fluid acidity. Hence, the dissolution process has likely been accommodated by syn-deformational, acidic and Fe-undersaturated fluid. The timing of this alteration event was probably related to the late stage of fluid flow after most of the hematite has been precipitated and the hydrothermal fluid was iron depleted and less oxidised.

The controlling structures during ore stage 2 that channelled hematite-mineralising and dolomite-leaching fluid were probably the same which were active during ore stage 1, i.e. BIF-basalt margins and faults (Fig. 7f). On a regional scale, potential cross-folding mechanisms between north–south F_2 and east–west F_{1b} (cf., Dalstra 1995) may create suitable dilatational zones for fluids entering and leaving the BIF. Such a geometric solution is quite likely, considering the conspicuous north–south alignment of ore bodies preferentially in large-scale fold hinge zones (Fig. 1c). The sequence of deformation events with orthogonally oriented, compressional cross-fold axes was probably important in terms of creating a plumbing system for mineralising fluids. Later stages of deformation involved brittle modifications of the BIF/basalt contacts, typically involving brecciation of magnetite–hematite ore (Fig. 7g), and formation of iron ore-basalt melange zones or breccias (Fig. 5f).

Ore stage 3: late magnetite and spcH overprint in BIF and iron ore

The last hypogene hydrothermal ore-forming stage is associated with the late-orogenic, brittle, compressional/transpressional stage (D_4). The D_4-fault system (Fig. 4d) created abundant space for quartz–dolomite–spcH veins in BIF and calcite–dolomite±spcH veins in basalt (Fig. 16d), which are prominent in the central northern W2 pit (Fig. 2). Earlier generated crosscutting faults were reactivated during D_4 as strike-slip faults.

Equation 5 in Table 2 describes a possible chemical reaction leading to ore stage 3 assemblage of spcH and dolomite. Acidic and oxidising fluid–rock conditions, probably similar to those during ore stage 2, accommodated the reaction. The similarity of spcH to lepH (Fig. 14e, f) suggests that the fluid chemistry was indeed comparable.

The associated Fe–dolomite-3, however, displays marked chemical differences to ore stage 1 Fe–dolomite-1 and ore stage 2 recrystallised Fe–dolomite-2. Although both generations show the same stoichiometry (Fig. 15a), transition metal contents are low in dolomite-3 when compared with dolomite-1 and dolomite-2 (<7 and >7 ppm, respectively, Fig. 15b). Also, the REE patterns are different in such that the LREE fractionation of late dolomite is stronger (lower $(La/Sm)_{PAAS}$) than early dolomite (Fig. 15b). Such a similarity of major element, but variable minor and trace element signatures for both carbonate generations indicates that the majority of dolomite was remobilised from pre-existing dolomite in altered BIF, veins and breccias, but the dissolution/precipitation agent (hydrothermal fluid) and physico-chemical conditions were subject to change.

Ore stage 3 is an ore-forming event that prepared rocks for supergene modification by adding extra carbonate to the BIF and creating a fault network that significantly increased permeability for supergene fluids to penetrate the rocks. However, high-grade spcH ore is not observed in Windarling, which is in contrast to the Koolyanobbing K deposit (Angerer and Hagemann 2010).

Ore stage 4: supergene-related goethite–martite ore formation

An intense supergene modification of hypogene hydrothermal ores is evident in Windarling (Fig. 16e). Supergene modification is structurally controlled by steep BIF-basalt margins and crosscutting D_4 faults. At the outer zones of all ore bodies, goethite precipitation is spatially related to pre-existing spcH–quartz–carbonate alteration (Fig. 7i). The two most important modifications during the supergene stage are the leaching and goethite replacement of carbonate and the oxidation of sulphides and magnetite to martite. Supergene-related modifications in the Windarling deposits are principally similar to other regions in the Southern Cross domain (Angerer and Hagemann 2010).

Interestingly, carbonate-altered BIF, hydrothermal magnetite–hematite ore below the supergene zone, and modified goethite–martite ore within the supergene zone, show similar element signatures with the exception of goethite–martite ore, which is MgO+CaO depleted, and Ni+Zn enriched (Fig. 13). Such a Ni+Zn enrichment in goethite–martite ore is most likely related to supergene martite, which typically shows such pattern in regolith (Anand and Gilkes 1984). This interpretation remains hypothetical, as element chemistry of the supergene martite is presently not available or not known.

Geochemical discrimination plots as predictive exploration tools

$(CaO+MgO+MnO)/Fe_2O_3$ versus SiO_2/Fe_2O_3

The entire hydrothermal-supergene geochemical alteration system of the Windarling W2 deposit can be effectively visualised in a simple major oxide discrimination diagram plotting $(CaO+MgO+MnO)/Fe_2O_3$ versus SiO_2/Fe_2O_3 (Fig. 17; Angerer et al. 2012). The alteration path is indicated by an arrow originating in (least-altered) siliceous BIF, shifting through low- to medium-grade Si-depleted Mg–Ca±Mn-

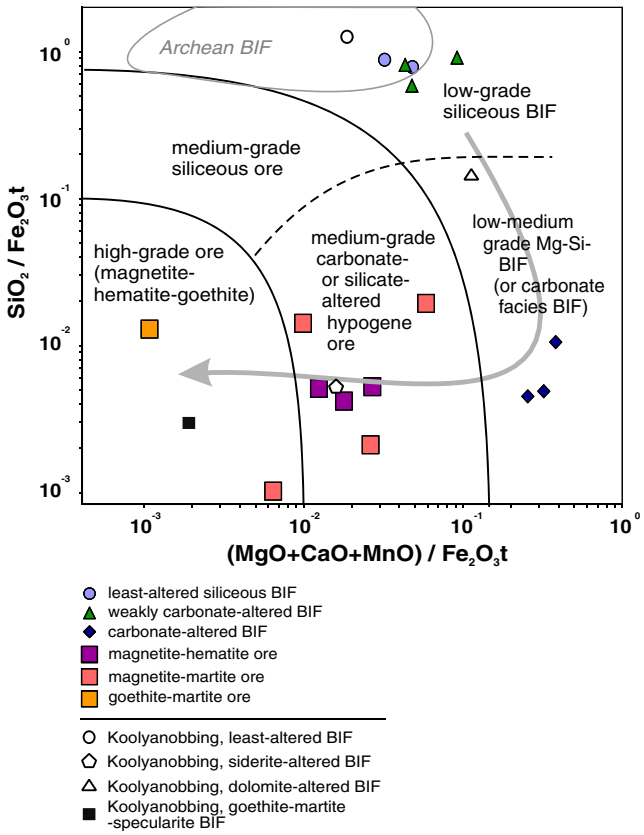

Fig. 17 Whole-rock geochemistry plot $(MgO+CaO+MnO)/Fe_2O_3$ versus SiO_2/Fe_2O_3. Shown are the field boundaries developed by Angerer et al. (2012) and average data for least-altered BIF, carbonate-altered BIFs and goethite–martite–spcH ore of the Koolyanobbing K and A deposit

altered BIF and high-grade Mg–Ca±Mn-bearing hydrothermal ore, to high-grade Si–Mg–Ca–Mn-depleted goethite–martite ore. This discrimination diagram may be used in exploration campaigns using standard assay programs, to estimate the potential existence of hypogene alteration zones in the prospect. It is valid for typical Algoma type BIF system lacking complex BIF stratigraphy, it has, however, its limitations in terranes, where shales, carbonates or other Mg–Ca–Mn-rich rocks are stratigraphically intercalated with BIF, such as in the Hamersley Province of Western Australia.

Sm/Yb and $(Gd/Gd^*)_{PAAS}$ versus Y/Ho

The binary Sm/Yb and Gd anomaly versus Y/Ho diagrams (modified after Alexander et al. 2008) are versatile diagrams for BIF-hosted iron ore genesis as they are able to depict alteration fluid signatures throughout the history of iron ore formation, from BIF formation to supergene modification (Angerer et al. 2012).

For the least-altered BIF, the mixing of principal fluid reservoirs (seawater and hydrothermal vent fluids) is expected (linear mixing line that connects seawater and hydrothermal fluids in Fig. 18a, b), but Y/Ho ratio in least-altered BIF deviated from that line ranging close to signatures of Archean mafic rocks (AMV) (values from Taylor and McLennan 1985). This indicates that mafic rocks must have modified vent fluids, which supports seafloor alteration in the footwall mafic rocks. This interpretation implies that no major fractionation of Y and Ho during fluid scavenging of basalts took place, a reasonable assumption considering that hydrothermal fluids typically obtain the chondritic Y/Ho of the igneous rocks from which they were released.

Carbonate-altered BIF has a lower Y/Ho ratio than least-altered BIF, ranging between two 'end-members' least-altered BIF and Archean mafic rocks. Whole-rock signatures are dominated by dolomite mineral chemistry, which seems to have collected an Archean mafic rock signature (Fig. 18c). The Sm/Yb ratios in late-stage dolomite-3 deviate from AMV towards Archean felsic igneous rocks and hydrothermal fluids. Granites have been postulated to play a significant source for hydrothermal fluids dominating the late-stage spcH ore formation at Koolyanobbing (Angerer et al. 2012).

The ratios Y/Ho and Sm/Yb (Fig. 18a, b) of supergene-modified goethite–martite and magnetite–martite ore clearly show same signatures as the hypogene carbonate-altered BIF and are largely distinct from least-altered BIF signatures. This depicts and therefore supports the goethite after carbonate replacement process, a very important stage in the ore genesis, without the necessity of direct petrographic evidence. Commonly, weathering processes do not change the Y/Ho ratio in rocks, which is envisaged by the fact that shales (i.e. weathered material) usually preserve the primary (typically chondritic) ratio of source rocks (cf., Bau 1996). Following Angerer et al. (2012), it is postulated that the carbonate alteration (i.e. Ca–Mg±Mn metasomatism of BIF) at Windarling, similar to the Koolyanobbing case, is a crucial 'ground preparation' for an effective supergene modification including goethite replacement and leaching of carbonate. This suggests that REE signature in supergene-modified iron ore may result in a successful 'fingerprint' of any hypogene alteration, and therefore a tracer for ore genesis.

Implications for BIF-hosted Yilgarn Craton and world-wide iron ore styles

BIF protoliths at Windarling and Koolyanobbing

Koolyanobbing is the closest studied relative to Windarling, and a comparison of both sets out to identify similarities and differences of ore formation processes throughout the Southern Cross domain. Stratigraphic thicknesses of BIF in Windarling are much thinner than at Koolyanobbing. Least-altered BIF in both deposits are petrographically and chemically quite different. The presence of crxH in

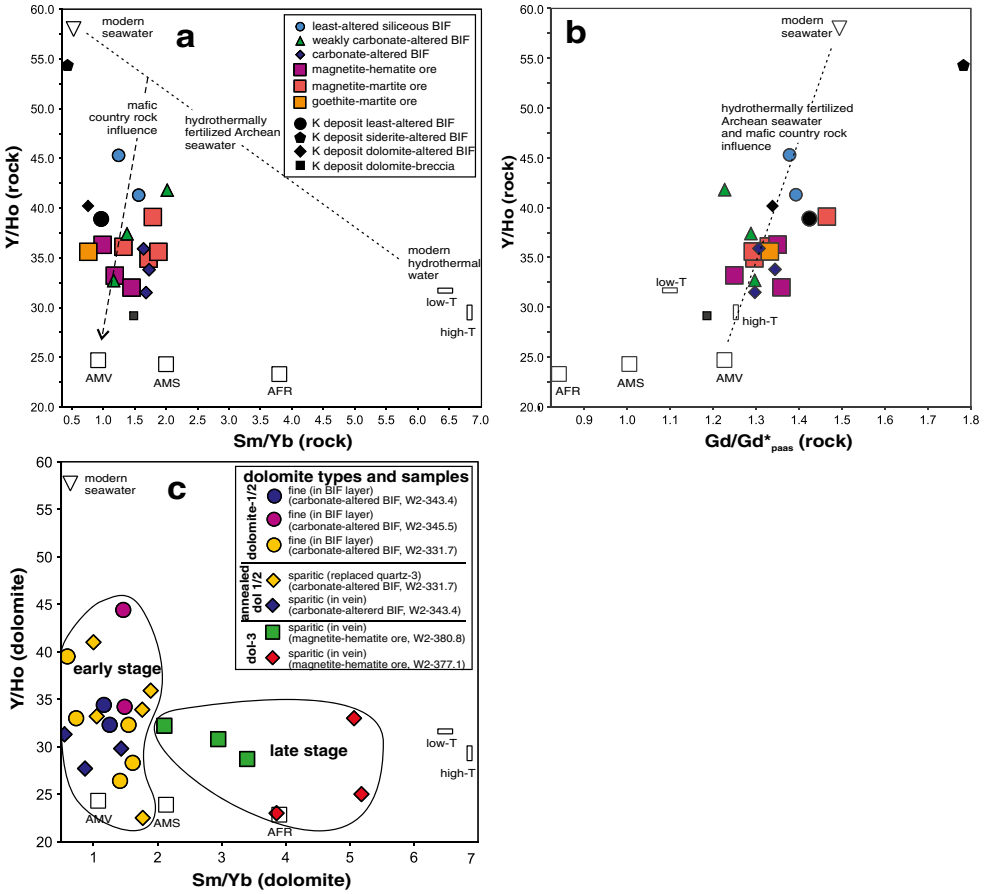

Fig. 18 Whole-rock geochemistry and mineral chemistry, REE-Y ratios **a** and **c** Sm/Yb versus Y/Ho and **b** (Gd/Gd*)$_{PAAS}$ versus Y/Ho. Shown are average values for modern seawater (>100 m depth) (Alibo and Nozaki 1999), modern hydrothermal water from seafloor vents (Bau and Dulski 1999), Archean mafic volcanic (*AMV*), Archean mudstones (*AMS*) and Archean Felsic rocks (*AFR*) (Taylor and McLennan 1985) and average data from key alteration zones at Koolyanobbing (Angerer et al. 2012)

Windarling BIF is related to regional sub-greenschist facies conditions. At Koolyanobbing, metamorphism is higher and metamorphic magnetite dominates. Here, however, structurally controlled crxH is clearly a distal hydrothermal alteration mineral associated with late-stage spcH (Angerer and Hagemann 2010; Angerer et al. 2012). At Windarling, carbonate and phosphate content in BIF and associated Mn, Ca, P, C, LOI, transition metals and REE concentrations is higher, but silicates (Al and K) and sulphides (S) lower (Fig. 11). In both Koolyanobbing and Windarling, BIF shows a typical Archean REE fractionation signature (Fig. 11). The magnetite element signature in M1 is similar to metamorphic magnetite in the K-deposit, except the Co/Ti ratio, which is distinctively higher (Fig. 14a). These data indicate that the BIF at Koolyanobbing and Windarling are not only different in stratigraphic facies and metamorphic grade, but also in textures, mineralogy and chemistry. Nevertheless, both variations were susceptible to carbonate-alteration and represent protoliths to high-grade iron ore.

Hypogene hydrothermal carbonate in BIF-related iron ore: towards the 'Yilgarn-style' iron ore system

For several major iron ore deposits in the Yilgarn Craton, a common hypogene alteration sequence including early carbonate–magnetite alteration, followed by intermediate magnetite ore formation, followed by late carbonate–hematite alteration has been established (Angerer et al. 2010). Final supergene modification and upgrade was mostly controlled by: (1) enhanced structural permeability via complex fault networks and (2) the various carbonate alteration zones in BIF. This is an important factor for the economic value of BIF-related iron ore deposits in the Yilgarn Craton. The ore-formation sequence for the Windarling deposits is compatible with the 'Yilgarn-style' paragenetic sequences (Angerer et al. 2010). Early (pre-ore) carbonate have also been observed in major BIF-related iron ore deposits at Koolyanobbing (Angerer and Hagemann 2010) and in the Beebyn deposit at the Weld Range (Duuring and Hagemann 2012b), at the Matthew Ridge prospect at Jack Hills (Maskell et al. 2012), and at the Mt. Gibson deposit (Lascelles 2006). There are only a few cases where carbonate alteration is not observed, such as at the Madoonga magnetite-vein-style deposit (Duuring and Hagemann 2012a) and various ore bodies within the Mt. Gibson deposit (Lascelles 2006). Where analysed, early carbonate at Windarling W2 and in Koolyanobbing K and A deposits are rich in Co–Ni–Zn and poor in REE when compared with later-stage carbonate, and Ni and Zn are anomalously elevated in hydrothermal iron oxides (this study and Angerer et al. 2012). Without further analytical evidences

from stable isotopes or fluid inclusions, this is preliminarily attributed to CO_3^--rich fluids interacting with mafic rocks (where they scavenge of Mg–Ca–Mn) prior to deposition of carbonates in the proximal BIF. This is supported by mafic rock-like Y/Ho and Sm/Yb ratios (Fig. 18). The source of early fluids is unknown and may be mafic rocks (devolatilisation), evaporites in the stratigraphy, or directly the ocean (supported by REE-Y ratios in Koolyanobbing: Angerer et al. 2012). Pre-ore carbonate alteration shows variable minerals types (siderite–magnesite in Koolyanobbing). The REE signatures, however, exhibit striking similarities in ΣREE, LREE fractionation and Eu anomalies. This may be an effect of the specific local mafic rock chemistries in both deposits. From high Y/Ho and low Sm/Yb ratios (Fig. 18a), it has been inferred that the early stage fluids were more seawater like.

Late-stage carbonate alteration, i.e. post-magnetite ore, is also common in many 'Yilgarn-style' iron ore and typically associated with spcH–quartz veins (Angerer et al. 2010). The chemistry of the late carbonate–spcH–quartz assemblage, compared with early carbonate–magnetite, is transition metal poor, REE-P rich with high Sm/Yb and low Y/Ho, and the associated hydrothermal fluid was oxidised and probably acidic. Based on this, it may be concluded that these hydrothermal fluids were less influenced by (transition metal rich) mafic and more by (REE rich) felsic igneous rocks and/or (oxidizing and acidic) meteoric water. The addition of carbonate to the deposit system in the late stage is possible but, based on the similar stoichiometry, pre-existing early Fe–dolomite in altered BIF may have been as well the source. When compared with its counterpart in the Koolyanobbing K-deposit, spcH in the W2 deposit has higher Ni, Zn and Co contents, which correlates with higher Ni, Zn and Co values in associated least-altered magnetite M1 (Fig. 14a, f). Therefore, local BIF being the source for Fe in spcH is likely. The high-field strength elements Al and Ti do not show this relative similarity between magnetite and carbonate, because they behave rather immobile and do not partition easily in carbonate.

The occurrences and expression of the late-stage carbonate–spcH alteration is heterogeneous, within iron ore 'camps' and across greenstone belts. For instance, the high-grade spcH ore is not developed in Windarling, although the hematite–dolomite–quartz–pyrite vein assemblage is very similar to the Koolyanobbing K deposit (Angerer et al. 2012). The Mt. Gibson deposit lacks spcH alteration. The variable scale and extent of hydrothermal spcH alteration may be related to the location of late-stage granites and large and extensive thermal convection and plumbing systems. For instance, the small scale of the D_4 faults and late-stage granites apophyses of the Pigeon Rock or Chatarie Well Granite in the Windarling Range (Fig. 1c) is in contrast to the large D_4 faults connecting the Koolyanobbing K and C deposits with the volumetrically significant Lake Seabrook granite (see Fig. 2 in Angerer and Hagemann 2010).

Syn-deformational hematite: a Quadrilátero Ferrífero-style mineralisation in the Yilgarn Craton?

Granoblastic–anhedral and lepH textures developed in deformed BIF and magnetite–hematite ore at Windarling are evidence for syn-deformational crystal–plastic deformation and growth of iron oxides. Because syn-hematite ductile strain is heterogeneously distributed in the BIF units, non-oriented masses of mplH formed as well, at the same time.

Such a syn-deformational hematite ore has not been described yet from iron ore deposits in the Yilgarn Craton but is known most prominently in the Neoarchean Cauê Formation in the Quadrilátero Ferrífero (QF) (Rosière et al. 2001; Rosière et al. 2008), also in higher metamorphosed BIF of central Nigeria (Mücke and Annor 1993) and North America (Brown 2008). Some fine lepidoblastic and granoblastic hematite in the 'Eastern High-Strain Domain' of the QF are strikingly similar to hematite in the W2 deposit. The Eastern High-Strain Domain, produced during the Brasiliano/Pan African event (500–600 Ma), is higher metamorphosed than the 'Western Low-Strain Domain', in which Trans-Amazonian age (2.1–2.0 Ga) anH after magnetite is well preserved (Rosière et al. 2008). In the Eastern High-Strain Domain, magnetite and anH recrystallised to lepH under syn-deformational, metamorphic, oxidative and fluid flow (Rosière et al. 2001, 2008).

Under geological strain rates (in the order of $10^{-14}s^{-1}$) crystal–plastic deformation of hematite can be expected to take place at temperatures above 300 °C (Rosière et al. 2001). Maximum regional burial metamorphism was, however, slightly lower grade (Dalstra et al. 1999). Therefore, the restricted distribution of (syn-deformational) hematite mineralisation, suggest the combination of local shear deformation and hot hydrothermal fluid circulation. This is actually similar to the Eastern High-Strain Domain, in which shear zone-related lepH mineralisation is also localised. Therefore, although significantly different in temperature and scale, Windarling and the high strain domains in the QF and Nigeria (amongst others) share a compressive structural environment during hematite mineralization with heterogeneously distribution of strain responsible for the variety of structures and fabrics.

Summary and conclusions

The deformation history recorded in the in the lower greenstone succession in the W2 iron ore deposit, Marda–Diemals greenstone belt, is compatible to the regional deformation

history and comprises three main deformation events (D_1 to D_4 with absence of D_3 in the deposit). The largest iron ore deposit in the Windarling Range, the W2 deposit, is a supergene-modified hypogene deposit, which shows a strong structural control on hydrothermal/metamorphic and supergene ore-forming stages. Archean hypogene iron ore formation in sub-greenschist facies metamorphosed 'least-altered' metachert–magnetite–crxH BIF took place in three distinct stages: (1) ore stage 1 is a syn- to post-metamorphic, syn-D_1, Fe–Ca–Mg–Co–Ni–P–REE metasomatism that caused local REE+Ni-rich Fe–dolomite–magnetite alteration in BIF. Hydrothermal alteration was controlled by brittle–ductile shear/fault zones along the various BIF-basalt contacts and crosscutting faults. Surrounding basalts were likely the main source of induced metals (Mg, Ca, Ni and Co) in altered BIF, whereas P and REE enrichment may have derived from distal granites. (2) Ore stage 2 is characterised by dolomite removal and replacement by fine-grained hematite under oxidized (acidic?) fluid-rock interaction. LepH, forming cleavages (S_1 and S_2) in magnetite–hematite ore, is a unique example for oxidised syn-compressional late-Archean iron ore formation in the Yilgarn. (3) Ore stage 3 hydrothermal spcH–Fe–dolomite–quartz alteration was related to a late-orogenic, brittle, compressional/transpressional stage (D_4). This metasomatic event locally modified BIF and magnetite–hematite ore in W2 but did not generate ore. (4) Ore stage 4 involved Mesozoic(?) to recent supergene enrichment and resulted in economically important martitisation of magnetite and goethite replacement of dolomite-quartz gangue. Hydroxidation and leaching reached depths of up to 200 m due to the vertical orientation of BIF and their restricted thicknesses, allowing for enhanced fluid penetration along BIF-basalt contacts.

Iron ore at Windarling and its broad similarity to Yilgarn-style ore deposits underpins the craton-wide communality of ore formation in similar lithostratigraphic and metamorphic settings. The similarity of ore textures at Windarling to deposits in completely different lithostratigraphic, metamorphic and age settings, i.e. the compressional high-strain deposits in Brazil (Quadrilátero Ferrífero) or Nigeria, shows how variable large-scale geological settings can produce very similar ore products, and how important it is to understand regional processes and fluids involved in iron ore formation in order to distinguish various ore geneses. This study demonstrates the importance of hydrothermal carbonate alteration as a 'ground preparation' for BIF-hosted iron ore in the Yilgarn Craton deposits. Ca–Mg–carbonate alteration in proximal mafic rock as observed in W2, may be a predictive exploration vector towards hypogene iron ore (cf., Dalstra and Guedes 2004). The usefulness of major, trace, and mineral geochemistry in ore genesis research and exploration is emphasised, as it allows differentiating chemical signatures of all major alteration stages and, to a certain extent, their fluid chemistry characteristics.

Acknowledgements This work has been funded and logistically supported by Cliffs Natural Resources Asia Pacific Iron Ore Ltd. The project was initiated by Nick Payne and Dave Fielding whose foresight and trust in using applied science as an aid for exploration is highly appreciated. The authors are grateful for the support from Cliffs Exploration/Resource Development team. Many thanks go to Andrew Ryan, Principal Exploration Geologist, and Rene Schellekens, Senior Mine Geologist at Cliffs' Windarling operation, for the logistical support and discussions in the mines and to Peter Fey who mapped Windarling region. Sarah Gilbert from CODES, University of Tasmania, is greatly acknowledged for her inductions at the Laser ablation system. We very much appreciate the thorough reviews of Carlos Rosière and Alexandre Raphael Cabral whose critique significantly improved the manuscript.

References

Ahmat AL (1986) Metamorphic patterns in the greenstone belts of the Southern Cross province, Western Australia. Geol Surv West Aust Prof Pap 19:1–21

Alexander BW, Bau M, Andersson P, Dulski P (2008) Continentally-derived solutes in shallow Archean seawater: rare earth element and Nd isotope evidence in iron formation from the 2.9 Ga Pongola Supergroup, South Africa. Geochim Cosmochim Acta 72(2):378–394

Alibo DS, Nozaki Y (1999) Rare earth elements in seawater: particle association, shale-normalization, and Ce oxidation. Geochim Cosmochim Acta 63(3–4):363–372. doi:10.1016/s0016-7037(98)00279-8

Anand RR, Gilkes RJ (1984) Mineralogical and chemical properties of weathered magnetite grains from lateritic saprolite. J Soil Sci 35:559–567

Angerer T, Hagemann SG (2010) The BIF-hosted high-grade iron ore deposits in the Archean Koolyanobbing Greenstone Belt, Western Australia: structural control on synorogenic- and weathering-related magnetite-, hematite-, and goethite-rich iron ore. Econ Geol 105(5):917–945. doi:10.2113/gsecongeo.105.5.917

Angerer T, Duuring P, Lascelles DF, Hagemann SG (2010) BIF-related iron ore in the Yilgarn Craton, Western Australia: geological setting and ore forming processes. Paper presented at the 5th International Archean Symposium, Perth, 5th–9th September 2010

Angerer T, Hagemann SG, Danyushevsky LV (2012) Geochemical evolution of the banded iron formation-hosted high-grade iron ore system in the Koolyanobbing Greenstone Belt, Western Australia. Econ Geol 107(4):599–644. doi:10.2113/econgeo.107.4.599

Barley ME, Pickard AL, Hagemann SG, Folkert SL (1999) Hydrothermal origin for the 2 billion year old Mount Tom Price giant iron ore deposit, Hamersley Province, Western Australia. Miner Deposita 34(8):784–789

Bau M (1996) Controls on the fractionation of isovalent trace elements in magmatic and aqueous systems: evidence from Y/Ho, Zr/Hf, and lanthanide tetrad effect. Contrib Mineral Petrol 123(3):323–333. doi:10.1007/s004100050159

Bau M, Alexander BW (2009) Distribution of high field strength elements (Y, Zr, REE, Hf, Ta, Th, U) in adjacent magnetite and chert bands and in reference standards FeR-3 and FeR-4 from the Temagami iron-formation, Canada, and the redox level of the

Neoarchean ocean. Precambrian Res 174(3–4):337–346. doi:10.1016/j.precamres.2009.08.007

Bau M, Dulski P (1996) Distribution of yttrium and rare-earth elements in the Penge and Kuruman iron-formations, Transvaal Supergroup, South Africa. Precambrian Res 79(1–2):37–55

Bau M, Dulski P (1999) Comparing yttrium and rare earths in hydrothermal fluids from the Mid-Atlantic Ridge: implications for Y and REE behaviour during near-vent mixing and for the Y/Ho ratio of Proterozoic seawater. Chem Geol 155(1–2):77–90. doi:10.1016/s0009-2541(98)00142-9

Bau M, Möller P (1993) Rare earth element systematics of the chemically precipitated component in early precambrian iron formations and the evolution of the terrestrial atmosphere–hydrosphere–lithosphere system. Geochim Cosmochim Acta 57(10):2239–2249. doi:10.1016/0016-7037(93)90566-f

Bekker A, Slack JF, Planavsky N, Krapez B, Hofmann A, Konhauser KO, Rouxel OJ (2010) Iron formation: the sedimentary product of a complex interplay among mantle, tectonic, oceanic, and biospheric processes. Econ Geol 105(3):467–508. doi:10.2113/gsecongeo.105.3.467

Beukes NJ, Gutzmer J, Mukhopadhyay J (2003) The geology and genesis of high-grade hematite iron ore deposits. Trans Inst Mining Metall Sect B-Appl Earth Sci 112(1):B18–B25. doi:10.1179/037174503225011243

Bolhar R, Van Kranendonk MJ (2007) A non-marine depositional setting for the northern Fortescue Group, Pilbara Craton, inferred from trace element geochemistry of stromatolitic carbonates. Precambrian Res 155(3–4):229–250. doi:10.1016/j.precamres.2007.02.002

Bowins RJ, Crocket JH (2011) Monazite, xenotime and REE minerals in Archean banded iron-formation from the Sherman and Adams mines, Ontario, Canada. Can Mineral 49(3):749–763. doi:10.3749/canmin.49.3.749

Brown PE (2008) Brief History of High-grade Iron Ore Mining in North America (1848–2008). In: Hagemann SG, Rosière CA, Gutzmer J, Beukes NJ (eds) Banded iron formation-related high-grade iron Ore, vol 15. Reviews in Economic Geology. pp 361–380

Cassidy KC, Champion DC, Krapez B, Barley ME, Brown SJA, Blewett RS, Groenewald PB, Tyler IM (2006) A revised geological framework for the Yilgarn Craton, Western Australia. Geological Survey of Western Australia, Record 2006/8

Chen SF, Wyche S (2001) Geology of the Bungalbin 1:100 000 sheet. Geological Survey of Western Australia, 1:100 00 Geological Series Explanatory Notes

Chen SF, Libby JW, Greenfield JE, Wyche S, Riganti A (2001) Geometry and kinematics of large arcuate structures formed by impingement of rigid granitoids into greenstone belts during progressive shortening. Geology 29:283–286

Chen SF, Riganti A, Wyche S, Greenfield JE, Nelson DR (2003) Lithostratigraphy and tectonic evolution of contrasting greenstone successions in the central Yilgarn Craton, Western Australia. Precambrian Res 127(1–3):249–266

Chin RJ, Smith RA (1983) Jackson: Geological Survey of Western Australia, 1:250,000 series Geological Map and Explanatory Notes

Cope IL, Wilkinson JJ, Boyce AJ, Chapman JB, Herrington RJ, Harris CJ (2008) Genesis of the Pic de Fon Iron Oxide Deposit, Simandou Range, Republic of Guinea, West Afrika. In: Hagemann S, Rosière CA, Gutzmer J, Beukes NJ (eds) Banded iron formation-related high-grade iron Ore, vol 15. Reviews in Economic Geology. pp 339–360

Dalstra HJ (1995) Metamorphic and structural evolution of greenstone belts of the Southern Cross–Diemals region of the Yilgarn Block, Western Australia, and its relationship to gold mineralisation. Ph.D. thesis, University of Western Australia

Dalstra H, Guedes ST (2004) Giant hydrothermal hematite deposits with Mg–Fe metasomatism: a comparison of the Carajas, Hamersley, and other iron ores. Econ Geol 99(8):1793–1800

Dalstra HJ, Ridley JR, Bloem EJM, Groves DI (1999) Metamorphic evolution of the central Southern Cross Province, Yilgarn Craton, Western Australia. Aust J Earth Sci 46(5):765–784

Danielson A, Möller P, Dulski P (1992) The europium anomalies in banded iron formations and the thermal history of the oceanic crust. Chem Geol 97(1–2):89–100. doi:10.1016/0009-2541(92)90137-t

Danyushevsky L, Robinson P, McGoldrick P, Large R, Gilbert S (2003) LA-ICPMS of sulphides: evaluation of an XRF glass disc standard for analysis of different sulphide matrixes. Geochim Cosmochim Acta 67(Supplement 1):A73

Duuring P, Hagemann SG (2010) High-grade iron mineralisation at the Beebyn deposit, Weld range, W.A. In: 5th Archean Symposium

Duuring P, Hagemann SG (2012a) Genesis of superimposed hypogene and supergene Fe ore bodies in BIF at the Madoonga deposit, Yilgarn Craton, Western Australia. Mineralium Deposita

Duuring P, Hagemann SG (2012b) Leaching of silica bands and concentration of magnetite in Archean BIF by hypogene fluids: Beebyn Fe ore deposit, Yilgarn Craton, Western Australia. Miner Deposita. doi:10.1007/s00126-012-0428-1

Dymek RF, Klein C (1988) Chemistry, petrology and origin of banded iron-formation lithologies from the 3800 MA isua supracrustal belt, West Greenland. Precambrian Res 39(4):247–302. doi:10.1016/0301-9268(88)90022-8

Gole MJ (1981) Archean banded iron-formations, Yilgarn Block, Western Australia. Econ Geol 76(7):1954–1974. doi:10.2113/gsecongeo.76.7.1954

Joly A, Miller J, McCuaig TC (2010) Archaean polyphase deformation in the Lake Johnston Greenstone Belt area: Implications for the understanding of ore systems of the Yilgarn Craton. Precambrian Res 177:181–198

Lascelles DF (2006) The Mount Gibson banded iron formation-hosted magnetite deposit: two distinct processes for the origin of high-grade iron ore. Econ Geol 101(3):651–666

Lepland A, Arrhenius G, Cornell D (2002) Apatite in early Archean Isua supracrustal rocks, southern West Greenland: its origin, association with graphite and potential as a biomarker. Precambrian Res 118(3–4):221–241. doi:10.1016/s0301-9268(02)00106-7

Lobato LM, Figueiredo e Silva RC, Hagemann SG, Thorne WS, Zuchetti M (2008) Hypogene alteration associated with high-grade banded iron formation-related iron Ore. In: Hagemann SG, Rosière CA, Gutzmer J, Beukes NJ (eds) Banded iron formation-related high-grade iron Ore, vol 15. Reviews in Economic Geology. pp 107–128

Maskell A, Duuring P, Hagemann SG (2012) Iron ore in the Methew ridge prospect, Jack Hills granite-greenstone belt. Aust J Earth Sci

McLennan SM (1989) Rare earth elements in sedimentary rocks: influence of provenance and sedimentary processes. Rev Mineral 21:169–200

Mücke A, Annor A (1993) Examples and genetic significance of the formation of iron oxides in the Nigerian banded iron-formations. Miner Deposita 28(2):136–145. doi:10.1007/bf00196338

Mücke A, Raphael Cabral A (2005) Redox and nonredox reactions of magnetite and hematite in rocks. Chemie der Erde-Geochem 65 (3):271–278. doi:10.1016/j.chemer.2005.01.002

Mueller AG, McNaughton NJ (2000) U–Pb ages constraining batholith emplacement, contact metamorphism, and the formation of gold and W–Mo Skarns in the Southern Cross Area, Yilgarn Craton, Western Australia. Econ Geol 95(6):1231–1257. doi:10.2113/95.6.1231

Nadoll P, Mauk JL, Hayes TS, Koenig AE, Hofstra AH, Box SE (2009) Geochemistry of magnetite from hydrothermal ore deposits and their host rocks in the Proterozoic Belt Supergroup, USA. Paper presented at the Proceedings of the 10th Biennial SGA Meeting of The Society for Geology Applied to Mineral Deposits Townsville Australia 17th–20th August 2009, Townsville

Nelson DR (2002) Compilation of geochronology data, 2001. Geological Survey of Western Australia Record 2002/2

Newman J, Mitra G (1994) Fluid-influenced deformation and recrystallization of dolomite at low temperatures along a natural fault zone, Mountain City window, Tennessee. Geol Soc Am Bull 106(10):1267–1280. doi:10.1130/0016-7606(1994)106<1267:fidaro>2.3.co;2

Nutman AP, Friend CRL (2006) Petrography and geochemistry of apatites in banded iron formation, Akilia, W. Greenland: Consequences for oldest life evidence. Precambrian Res 147(1–2):100–106. doi:10.1016/j.precamres.2006.02.005

Ohmoto H (2003) Nonredox transformations of magnetite–hematite in hydrothermal systems. Econ Geol 98:157–161

Ohmoto H, Watanabe Y, Yamaguchi KE, Naraoka H, Kakegawa T, Haruna M, Hayashi K, Kato Y (2006) Chemical and biological evolution of early Earth: constraints from banded iron-formations. In: Kesler S, Ohmoto H (eds) Evolution of the Atmosphere, Hydrosphere, and Biosphere on Early Earth: Constraints from Ore Deposits. Geological Society of America Memoir, 196, pp 269–289

Planavsky N, Bekker A, Rouxel OJ, Kamber B, Hofmann A, Knudsen A, Lyons TW (2010) Rare earth element and yttrium compositions of Archean and Paleoproterozoic Fe formations revisited: new perspectives on the significance and mechanisms of deposition. Geochim Cosmochim Acta 74(22):6387–6405. doi:10.1016/j.gca.2010.07.021

Portman (2008) Annual report 2007, Croatia

Qiu YM, McNaughton NJ, Groves DI, Dalstra HJ (1999) Ages of internal granitoids in the Southern Cross region, Yilgarn Craton, Western Australia, and their crustal evolution and tectonic implications. Aust J Earth Sci 46(6):971–981

Rasmussen B, Fletcher IR, Muhling JR, Thorne WS, Broadbent GC (2007) Prolonged history of episodic fluid flow in giant hematite ore bodies: evidence from in situ U–Pb geochronology of hydrothermal xenotime. Earth Planet Sci Lett 258(1–2):249–259

Riganti A, Chen SF (2002) Geology of the Jackson 1:100 000 sheet. Geological Survey of Western Australia, 1:100 00 Geological Series Explanatory Notes

Rosière CA, Siemes H, Quade H, Brokmeier H-G, Jansen EM (2001) Microstructures, textures and deformation mechanisms in hematite. J Struct Geol 23(9):1429–1440. doi:10.1016/s0191-8141(01)00009-8

Rosière CA, Spier CA, Rios FJ, Suckau VE (2008) The itabirites of the Quadrilátero Ferrífero and related high-grade iron ore deposits: an overview. In: Hagemann SG, Rosière CA, Gutzmer J, Beukes NJ (eds) Banded iron formation-related high-grade iron Ore, vol 15. Reviews in Economic Geology. pp 223–254

Figueiredo e Silva RC, Lobato LM, Rosiere CA (2008) A hydrothermal origin for the Jaspilite-Hosted Giant Sierra Norte Deposits in the Cajajas Mineral Province, Para State, Brazil. In: Hagemann S, Rosière CA, Gutzmer J, Beukes NJ (eds) Banded iron formation-related high-grade iron Ore, vol 15. Society of Economic Geologists, pp 255–290

Figueiredo e Silva RC, Lobato LM, Hagemann SD, L. (2009) Laser-ablation ICP-MS analyses on oxides of hypogene iron ore from the giant Serra Norte jaspilite-hosted iron ore deposits, Carajás Mineral Province, Brazil. Paper presented at the Proceedings of the 10th Biennial SGA Meeting of The Society for Geology Applied to Mineral Deposits, Townsville, Australia, 17th–20th August 2009

Sun SS, McDonough WF (1989) Chemical and Isotopic Systematics of oceanic basalts: implications for Mantle Composition and Processes. Spec Publ Geol Soc Lond 42:313–345

Taylor SR, McLennan SM (1985) The continental crust: its composition and evolution. Blackwell, Oxford

Taylor D, Dalstra HJ, Harding AE, Broadbent GC, Barley ME (2001) Genesis of high-grade hematite orebodies of the Hamersley province, Western Australia. Econ Geol Bull Soc Econ Geol 96(4):837–873

Wyche S, Chen SF, Greenfield JE, Riganti A (2001) Geology of the Johnston 1:100 000 sheet. Geological Survey of Western Australia, 1:100 00 Geological Series Explanatory Notes